

The Structure of pH Dependent Block Copolymer Micelles: Charge and Ionic Strength Dependence *

Albert S. Lee, Alice P. Gast

Department of Chemical Engineering, Stanford University, Stanford CA 94305-5025

Vural Bütün, Steven P. Armes

Department of Chemistry, University of Sussex, Falmer, Brighton, BN1 9RH UK

John A. Pople

Stanford Synchrotron Radiation Laboratory, Stanford Linear Accelerator Center,
Stanford University, Stanford, CA 94309

Abstract

We characterize the structures of various polyelectrolyte block copolymer micelles in dilute aqueous solution as a function of pH and ionic strength. The block copolymers carry a common core block 2-(diethylamino) ethyl methacrylate (DEAEMA) and one of three coronal blocks: 2-(dimethylamino) ethyl methacrylate (DMAEMA), polyethylene oxide (PEO), and DMAEMA whose side-chain amine groups are selectively quaternized with benzyl chloride (Q-DMAEMA). The PEO-DEAEMA, DMAEMA-DEAEMA, and Q-DMAEMA-DEAEMA copolymers form micelles with electrostatically neutral, weakly charged, and highly charged coronae, respectively. We adjust the fractional charge α on the DEAEMA and DMAEMA blocks by adjusting the solution pH. For DMAEMA-DEAEMA micelles increasing the fractional charge α swells the micelle corona while decreasing the aggregation number due to electrostatic repulsions. The decrease in aggregation number is also observed with increasing α for the PEO-DEAEMA and Q-DMAEMA-DEAEMA micelles, due to electrostatic repulsions between the hydrophobic DEAEMA blocks. Increasing the ionic strength causes the DMAEMA-DEAEMA micelle corona to shrink as the salt screens electrostatic repulsions within the corona. In all three copolymers increases in the ionic strength causes the micelle aggregation number to increase by screening the electrostatic repulsions between chains. Trends in the corona thickness with varying fractional charge and ionic strength are compared with a number of theoretical models providing additional insight into the micelle structure.

Keywords

micelles; polymers; electrostatic interactions; block copolymers; micelle solutions; SAXS; pH dependent structure; molecular architecture

Submitted to Macromolecules

* Work supported by Department of Energy contract DE-AC03-76SF00515

The Structure of pH Dependent Block Copolymer Micelles: Charge and Ionic Strength Dependence

Albert S. Lee[†], Vural Bütün^{‡§}, Steven P. Armes[†], John A. Pople^{*†} and Alice P. Gast^{*†}

Department of Chemical Engineering, Stanford University, Stanford, CA 94305-5025; School of Chemistry, Physics and Environmental Science, University of Sussex, Brighton BN1 9QJ, E. Sussex, UK

* To whom correspondence should be addressed.

† Stanford University and Stanford Synchrotron Radiation Laboratory.

‡ University of Sussex.

§ Current address: Faculty of Arts and Science, Department of Chemistry, Osmangazi University, 26480, Eskisehir, Turkey.

Abstract

We characterize the structures of various polyelectrolyte block copolymer micelles in dilute aqueous solution as a function of pH and ionic strength. The block copolymers carry a common core block, 2-(diethylamino) ethyl methacrylate (DEAEMA) and one of three coronal blocks: 2-(dimethylamino) ethyl methacrylate (DMAEMA), polyethylene oxide (PEO), and DMAEMA whose side chain amine groups are selectively quaternized with benzyl chloride (Q-DMAEMA). The PEO-DEAEMA, DMAEMA-DEAEMA, and Q-DMAEMA-DEAEMA copolymers form micelles with electrostatically neutral, weakly charged, and highly charged coronae, respectively. We adjust the fractional charge α on the DEAEMA and DMAEMA blocks by adjusting the solution pH. For DMAEMA-DEAEMA micelles increasing the fractional charge α swells the micelle corona while decreasing the aggregation number due to electrostatic repulsions. The decrease in aggregation number is also observed with increasing α for the PEO-DEAEMA and Q-DMAEMA-DEAEMA micelles, due to electrostatic repulsions between the hydrophobic DEAEMA blocks. Increasing the ionic strength

causes the DMAEMA–DEAEMA micelle corona to shrink as the salt screens electrostatic repulsions within the corona. In all three copolymers increases in the ionic strength causes the micelle aggregation number to increase by screening the electrostatic repulsions between chains. Trends in the corona thickness with varying fractional charge and ionic strength are compared with a number of theoretical models providing additional insight into the micelle structure.

1 Introduction

Amphiphilic block copolymers have been a subject of much technological and scientific interest because of their interesting solution properties. One of their interesting properties is their associative behavior, where the insoluble parts coalesce to minimize their contact with the solvent and the molecules aggregate to form micelles. The insoluble blocks aggregate to form a dense core, and the soluble blocks extend out into the solvent to form a corona.^{1,2} These micelles can assume various shapes, ranging from worm-like to spherical micelles.^{3,4} The behavior of uncharged diblock copolymers is fairly well understood experimentally and theoretically in terms of their structure and micellar associative behavior.^{5–17}

More recently theoretical models describing the structure of charged polyelectrolyte micelles have been increasing. Many of the theories describe spherical micelles with a charged corona and an electrostatically neutral core.^{18–29} While the theories for neutral micelles draw from analogies with semidilute polymer solutions, semidilute polyelectrolyte theory is not as well established and the charged micelles are more difficult to model. A spherical micelle can be thought of a polymer brush at a curved interface, where polymer chains are end-grafted

at a solid-liquid interface, and models of charged polymer brushes at a flat interface offer additional insight into the structure of the charged micelle corona. Theories for both micelles and polymer brushes have been developed for so-called quenched polyelectrolytes where the charges are fixed along the polymer chain,^{18–26} as well as for annealed systems where the charge distribution is allowed to vary along the polymer chain, as in a weak polyacid or polybase.^{26–29}

While the number of theories has been increasing the experimental works remain relatively few. For both quenched and annealed polyelectrolyte micelles as well as brushes the addition of salt is found to screen electrostatic interactions in the micelle corona or brush to cause the thickness to decrease.^{25,30–36} Addition of salt also promotes larger micellar aggregation numbers or polymer brushes with higher grafting densities because of electrostatic screening of repulsions between chains.^{30,33,37} For the annealed polyelectrolyte micelles and brushes the pH controls the degree of charge in the micelle corona or polymer brush and can induce swelling due to electrostatic repulsions.^{35,37–40}

One specific class of polyelectrolyte micelles are pH-sensitive micelles where the copolymers aggregate to form micelles when the pH is adjusted beyond the critical value.^{41,42} In general, aqueous copolymer systems have been difficult to prepare and to work with, often requiring a co-solvent such as methanol or THF to adequately dissolve the polymers to form relatively stable, uniform micelles.⁴³ In contrast, the pH sensitive copolymers can be dissolved as unimers by adjusting the pH and then slowly titrated to form relatively uniform micelles without the use of a co-solvent. The associative behavior of neutral copolymers has traditionally been characterized by the *cmc*, and these pH sensitive copolymers can in addition be characterized by the critical pH denoted pH^* or the critical fractional charge α^*

where the copolymer fractional charge α depends on the pH and takes values $0 \leq \alpha \leq 1$. Another interesting aspect of the pH sensitivity is that these copolymers could serve as a model for a delivery system, where the solute encapsulated in the micelle cores is released as the micelles break apart when they reach a target pH. The pH induced release of a solute is potentially useful in drug delivery^{41,44-46} or environmental remediation systems.⁴⁷

Recently Armes and coworkers⁴⁸⁻⁵¹ have developed a series of novel pH sensitive block copolymers which form micelles having coronae with various electrostatic properties. Among these novel block copolymers are 2-(dimethylamino) ethyl methacrylate-*block*-2-(diethylamino) ethyl methacrylate (DMAEMA-DEAEMA), polyethylene oxide-*block*-2-(diethylamino) ethyl methacrylate (PEO-DEAEMA), and DMAEMA-DEAEMA with the DMAEMA block selectively quaternized with benzyl chloride (Q-DMAEMA-DEAEMA). The three copolymers contain the same hydrophobic DEAEMA block, and their chemical structures are shown in Figure 1. Under acidic conditions, the amine groups on the DEAEMA side chains are protonated, causing the copolymers to become hydrophilic and to remain as unimers in solution. The subsequent addition of base deprotonates the side chains, causing the DEAEMA block to become hydrophobic. Above the critical pH the copolymers aggregate to form micelles. The DEAEMA block forms the micelle core while the hydrophilic DMAEMA, PEO, or Q-DMAEMA block extends into the solvent to form the micelle corona. The primary difference between the three copolymers is in the electrostatic properties of the hydrophilic block forming the micelle corona, where we have electrostatically neutral, weakly charged, and strongly charged hydrophilic blocks from PEO, DMAEMA, and Q-DMAEMA, respectively. An interesting aspect of the DMAEMA-DEAEMA micelles is that the fractional charge α on the DMAEMA block can be varied by adjusting the solution pH, such

that the degree of charge in the micelle corona can be varied. The DMAEMA block acts as a weak polybase and forms a micelle corona expected to behave as an annealed brush, whereas in Q-DMAEMA–DEAEMA the charges are fixed and the coronal chains are quenched polyelectrolytes.

In this work we seek to study these three copolymers to further the understanding of polyelectrolyte block copolymer micelles with varying pH and ionic strength. To our knowledge, a unique aspect of this work is that we study the charge dependence not only of the hydrophilic coronal block but also of the hydrophobic core block. In addition, there have been few attempts in the literature^{25,36,39,40,52} to directly compare experimental results with theoretical models for polyelectrolyte micelles and brushes, and our work contributes towards filling this gap.

2 Theoretical Models from the Literature

2.1 Electrostatically Neutral Micelles

A range of mean field and self-consistent field models have been developed which describe the structure of electrostatically neutral micelles. The star-like micelle scaling model developed by Vagberg *et al.*⁶ and Witten and Pincus,¹⁷ based on the work of Daoud and Cotton¹¹ describes the micelle as a spherical core surrounded by a shell of chains extending out into the solvent, as in a star, shown in Figure 2a. The model depicts the coronal shell as a series of connected blobs whose sizes increase with increasing distance r away from the core. The

expression

$$\xi(r) = N_{\xi}^{\nu} a = 4r/f^{1/2} \quad (1)$$

describes the blob size $\xi(r)$, where f is the number of chains per micelle or arms in the star, a is the statistical segment length in the corona, ν is the Flory exponent, and N_{ξ} is the number of segments per blob. The micelle density profile $\rho(r)$ as a function of distance r from the micelle center can be obtained from Equation 1. Integration of the density profile over the micelle volume and matching with the known total number of monomers within this volume gives expressions for the core and micelle radii, as described previously.⁴² The radius of gyration R_g measured by SANS is evaluated from the second moment of the scattering length density^{6,7,42} $\rho^N(r)$.

2.2 Quenched Polyelectrolytes

Misra and coworkers¹⁸ were among the first to pioneer the development of a theoretical model for polyelectrolyte brushes, where they extend the Milner-Witten-Cates self consistent field (SCF) theory⁵³ to calculate polyelectrolyte brush profiles and heights at varying ionic strengths. Since then, a number of models have been developed for polyelectrolyte micelles.

Argillier and Tirrell²⁰ extended the mean field theory of Marques, Joanny and Leibler¹³ for quenched polyelectrolyte brushes. The polyelectrolyte chains of N segments are anchored at a dimensionless density σ to a flat solid-liquid interface. The brush thickness L is determined by a minimization of the sum of the elastic and osmotic free energies. As added salt and counterions contribute to the osmotic free energy the following dependence on the added salt

concentration C_s is found from the energy minimization

$$L \sim N(a^2\sigma)^{1/3}C_s^{-2/3} \quad (2)$$

Here the chain grafting density σ can be calculated for spherical micelles as $\sigma = f/4\pi R_c^2$.

Dan and Tirrell²¹ find the same scaling from a Daoud-Cotton model for a flat interface. At a highly curved interface, the corona thickness

$$L \sim aN_s^{3/5}\frac{f^{1/5}}{\phi_s^{2/5}} \quad (3)$$

has a weaker salt dependence than in the flat brush case and has an explicit dependence on the aggregation number f . In this treatment the salt concentration is expressed as the volume fraction ϕ_s .

Russel and coworkers present a comprehensive review of theories describing the ionic strength dependence of quenched polyelectrolyte brushes²⁵ and comparing them with their experimental measurements of the ionic deswelling of polymer brushes at curved interfaces.^{24,25} In addition, Russel and coworkers develop a theoretical description based on a modification of the Daoud-Cotton scaling model. In their model the blob size $\xi \sim N_\xi^{3/5}a(v_{ex}/a)^{1/5}$ where N_ξ is the number of segments per blob and the excluded volume parameter v_{ex} is valid for good solvent conditions. This blob model provides asymptotic expressions for the corona thickness L in the planar and spherical cases. The ionic strength dependence appears in both the segment length a and excluded volume v_{ex} , given by Odijk and Fixman^{54,55} as $a \sim 1/l_b\kappa^2$ and $v_{ex} \sim a^2\kappa^{-1}$. The Bjerrum length l_b is defined as $l_b = e^2/4\pi\epsilon k_B T$ where e is the electron charge and ϵ is the solvent dielectric constant. The Debye screening length $\kappa^{-1} = (8\pi l_b C_s z^2 N_A)^{-1/2}$ describes the electrostatic screening due to the ions where z is the valency of the ions and N_A is Avogadro's constant. With $\kappa \sim C_s^{1/2}$,

a and v_{ex} scale as C_s^{-1} and $C_s^{-3/2}$, respectively, and substitution into the blob model gives the scaling $L \sim \sigma^{1/3} C_s^{-1/2}$ for the planar case. When the segment length dependence on ionic strength is ignored and v_{ex} is retained, as in Pincus' description of polyelectrolyte brushes, the scalings become $L \sim \sigma^{1/3} C_s^{-1/6}$ and $L \sim R_c^{2/5} \sigma^{1/5} C_s^{-1/10}$ for the planar and spherical cases, respectively. Russel and coworkers find that these exponents agree with their experimental findings.²⁵

A different scaling exponent for the ionic strength dependence was found by Pincus¹⁹ from a mean-field approximation balancing elastic and osmotic forces, giving

$$L \sim Na\sigma^{1/3}(aC_s)^{-1/3} \quad (4)$$

The mean field force balance gives a weaker C_s scaling than the mean field energy minimization of Argillier and Tirrell. In addition, Pincus found the following dependence of the layer thickness on the degree of charge α

$$L \sim \alpha^{1/2} Na \quad (5)$$

Zhulina and Borisov²⁶ also used force balances to find the dependence of planar brushes on fractional charge α , and they extend their treatment to include brushes at cylindrical and spherical interfaces. For quenched brushes they present a phase diagram where different brush height scalings occur. In the osmotic brush, or OsB regime, the charge density is high, such that most of the counterions are found within the brush where they cause an osmotic force balanced by the elastic force. In the neutral brush, or NB regime, α is small, and the brush is described by the theories and models cited above. Zhulina and Borisov give an expression for the neutral brush thickness L at a spherical interface

$$L \sim N^{1/2} a (R_c^2 \sigma)^{1/4} \quad (6)$$

For the quenched osmotic brush grafted on either a flat or spherical surface, the scaling follows the Pincus scaling in Equation 5. The electrostatic blob for this case is defined such that one charge is found in each blob, and the blob size scales as $\xi \sim a\alpha^{-1/2}$. These electrostatic blobs are not necessarily touching between chains, as shown in Figure 2b in contrast with the star-like micelle model. An inner region of the micelle corona is also described where the blobs are packed as in the star-like micelle model, and its boundary R_n occurs where the concentration of segments in the packed blob equals that of the electrostatic blob.

Khokhlov and coworkers²³ also develop a model for quenched polyelectrolyte brushes at flat and spherical interfaces. In their treatment of charged micelles a similar picture is given as Figure 2b, where the corona is described as a series of electrostatic blobs of size $\xi \sim aN_\xi^{3/5}$ for good solvent conditions. The number of segments per blob N_ξ is constrained such that the electrostatic repulsion between two adjacent blobs equals the thermal energy $k_B T$. The blobs are of equal size and the predicted brush thickness is simply the sum of blob diameters, giving

$$L \sim N_s (l_b/a)^{2/7} \alpha^{4/7} a \quad (7)$$

To predict micelle aggregation numbers the total free energy summing the free energy of the core, the core-corona surface energy, and the elastic and electrostatic energy of the blobs in the corona is minimized. For micelles with appreciable charge, the core-corona surface and the electrostatic energies dominate, and minimization gives a scaling for f

$$f \sim (\gamma a^2)^3 \frac{N_c^2}{N_s^3 \alpha^3} \quad (8)$$

where N_c and N_s are the number of segments per block copolymer chain for the core and corona, respectively and γ is the surface tension associated with the core-corona interface

normalized with $k_B T$.

The models for quenched polyelectrolytes apply to a variety of conditions, as summarized in Table 1.

2.3 Annealed Polyelectrolytes

The case of annealed polyelectrolytes is much more complicated than the quenched case. For brushes composed of weak polyacids or polybases the charges along the polymer chains are allowed to anneal to adjust to the local acid or base concentrations. This annealing causes the charge distribution in the brush to vary with distance from the grafting interface.

Israëls, Leermakers and Fleer²⁷ use a numerical SCF model to describe the structure and charge distribution of a planar brush with varying pH and ionic strength. The numerical analysis shows that the fractional charge increases with distance from the grafting surface.

Birshtein and coworkers²⁸ developed a mean field model to describe a weak polyacid brush at a flat interface in terms of the ionic strength, grafting density, and charge. Electroneutrality requires the ions in the brush to balance the charges along the chains, and the ions follow a Boltzman distribution. A force balance between elastic and electrostatic forces provides the polymer concentration ϕ in the brush which when combined with the charge distribution gives

$$L \sim N a^{4/3} \sigma^{-1/3} \left(\frac{\alpha_b}{1 - \alpha_b} (C_H^* + C_s) \right)^{1/3} \quad (9)$$

for low ion concentrations and $\alpha \ll 1$. Here α_b and C_H^* are the fractional charge and H^+ concentration in bulk solution. At high ion concentrations the thickness scales as

$$L \sim N (a^2 \alpha^2 \sigma C_s^{-1})^{1/3} \quad (10)$$

which is similar to the quenched brush described by Equation 4, except with an additional factor, $\alpha^{2/3}$. At high salt the brush effectively acts as a quenched brush.

Leermakers and coworkers²⁹ developed a picture of a weak polyacid brush using an analytical SCF model. The acid-base equilibrium and electroneutrality conditions in the brush are combined with a Boltzmann distribution of ions; minimization of the brush free energy provides an analytical solution for the charge distribution. The brush thickness at high ionic strength follows the same scaling as that of Birshtein and coworkers, again indicating that salt causes the brush to resemble a quenched brush. The asymptotic solutions for the thickness of the osmotic brush is more complicated,

$$L \sim Na\sqrt{-\ln(1 - \alpha_b) - \alpha_o} \quad (11)$$

where α_o is

$$\alpha_o \sim \left(\frac{1}{\sqrt{6}} \frac{2 + \pi \Phi^+}{2\pi} \frac{\alpha_b}{\sigma(1 - \alpha_b)} \right)^{2/3} \quad (12)$$

and Φ^+ is the cation concentration.

Zhulina and Borisov²⁶ extended their model for quenched polyelectrolyte brushes described in the previous section to describe weak polyacid brushes. The treatment assumes no salt added such that all ions are H^+ ions. In this case a Boltzmann distribution is not needed, and the electroneutrality condition and acid-base equilibrium suffice to obtain the charge distribution which increases with distance from the micelle core. If the blobs are defined such that each blob contains one charge, the blob size is predicted to decrease with distance from the core as the number of charges increases. Zhulina and Borisov also describe an internal sublayer, and their description of the annealed micelle corona is depicted in Figure 2c. For the case with no internal sublayer, the segment concentration profile in

the brush, in conjunction with the charge distribution are used to obtain an expression for the corona thickness L

$$L \sim aN_s^3(Ka^3)/\sigma R_c^2 \quad (13)$$

Here K is the acid dissociation constant. Interestingly, the layer thickness is not directly dependent on the fractional charge in the bulk, α_b .

The theories for annealed brushes are summarized in Table 2. Many theoretical models describing quenched and annealed brushes under a variety of conditions have been described in this section. We seek to place our experimental findings in the context of these models and use these models to gain a better understanding of the structure and interactions in the micelle corona.

3 Experimental Methods

3.1 Materials

Block copolymers of 2-(dimethylamino) ethyl methacrylate-*block*-2-(diethylamino) ethyl methacrylate (DMAEMA-DEAEMA) and polyethylene oxide-*block*-2-(diethylamino) ethyl methacrylate (PEO-DEAEMA) were synthesized at Sussex. The details of the synthesis are reported elsewhere.^{48,49} A third copolymer sample (Q-DMAEMA-DEAEMA) was produced at Sussex by selectively quaternizing the DMAEMA amine groups in the DMAEMA-DEAEMA copolymer with benzyl chloride. DMAEMA and DEAEMA homopolymers were also synthesized, and PEO homopolymer was purchased from Polysciences. In addition, a bet-DMAEMA homopolymer was synthesized, where the DMAEMA homopolymer was

betainized using propane-1,3-sultone.^{48,50} The copolymer and homopolymer properties are listed in Table 3.

Gel permeation chromatography was used to measure molecular weights and polydispersity, except for the case of Q-DMAEMA–DEAEMA, where the molecular weight was calculated from the NMR data showing 100% quaternization of the DMAEMA block. NMR measurements were also used to determine the relative mole fractions of each block. The solid state density of DEAEMA homopolymer, 1.046 g/ml, was measured with helium pycnometry.

We prepared each sample by dissolving the copolymer in Milli-Q deionized water with enough HCl to match the monomer concentration of amine groups. In this way, complete molecular dissolution of the copolymers is ensured. Copolymer concentrations range from 0.001 to 0.01 g/ml. The copolymer solutions are filtered through either a 0.2 μ Whatman Anotop or 0.45 μ Gelman Nylon syringe filter before micelle formation. In the case of Q-DMAEMA–DEAEMA aggregates are detected via light scattering even at low pH, and a series of filtrations were required to minimize these aggregates. The Q-DMAEMA–DEAEMA solutions were first filtered through 0.45 μ Gelman Nylon and 0.1 μ Whatman Anotop syringe filters. These filtered solutions were then ultrafiltered using Millipore Ultrafree-CL 300,000 NMWL filters at 1,700 rpm (480 G) in a Beckman GPR centrifuge for 3.5 hours. Prior to ultrafiltration of the Q-DMAEMA–DEAEMA solutions, pure water was flushed through the filters.

For the titrations, standardized acid and base solutions of HCl and KOH were each prepared at 1 M and 0.1 M concentrations. The dissolved copolymer solutions were slowly titrated to higher pH using KOH and gently agitated or left to equilibrate overnight before

experiments were performed.

3.2 Potentiometric Titrations

A Rainin motorized pipette (EDP Plus) with a 100 μl liquid end was used to deliver known amounts of standardized HCl or KOH to the samples while the pH was monitored on an Orion 611 pH meter with a semi-micro combination electrode (Orion Ross 8103). Due to the tendency of the pH to drift over many minutes, the accuracy of the pH is estimated to be approximately 0.05 pH units. Titration curves were generated by first titrating the solution to low pH with 1 M HCl to ensure complete dissolution of the copolymer, and then measuring the pH in 10 to 100 μl increments of 0.85 M or 0.085 M KOH.

As HCl and KOH are added during the titrations, K^+ and Cl^- ions are unavoidably added. The effective amount of KCl added during the titrations is taken into account for salt dependent measurements. During polymer dissolutions, just enough HCl is added to protonate all the amine groups, ensuring complete dissolution and minimizing the amount of effective KCl added; thus solutions with lower polymer concentrations have lower effective salt concentrations.

We define α as the ratio C_H/C_m , where C_H is the effective concentration of added HCl and C_m is the monomeric concentration of polymer chains. When defined in this way, α approximates the degree of protonation, or the fraction of amine groups in the chain protonated, assuming that all the added protons protonate the amine groups. In some cases the calculations for C_H needed to be adjusted to cause the $\alpha = 0$ and $\alpha = 1$ values to occur at the inflections of the titration curves. We define α^* as the critical α , below which micelles

form. Similarly, pH^* is the critical pH above which micelles form.

We can model the titration of the copolymer solution as the titration of a monoprotic weak acid buffer with a strong base, where the copolymer comprises monomers having an average pK_a . Using average pK_a values obtained from the titrations described above, model titration curves can be calculated.⁵⁶ Titration curves of DMAEMA–DEAEMA, PEO–DEAEMA, and Q-DMAEMA–DEAEMA copolymers are shown in Figure 3, along with the calculated titration curves for pK_a values of 7.2, 6.8, and 7.1 for the three copolymers, respectively. The varying salt conditions and difference between the DMAEMA and DEAEMA pK_a are responsible for the slight differences between the three copolymer pK_a values. The PEO–DEAEMA and Q-DMAEMA–DEAEMA micelles remain in solution even at high pH. The model and experimental titration curves as a function of α are shown in Figure 3b. The regions where $\alpha < 0$ or $\alpha > 1$ are where the acid or base concentration exceeds that required to fully deprotonate or fully protonate the chain. Good agreement between the model calculations and the measured data validates our assumption that effectively all of the H^+ ions from the added HCl protonate the amine groups.

3.3 Turbidity Measurements

Turbidity measurements were conducted by shining a laser through copolymer solutions and measuring the scattered light intensity at 90° relative to the incident beam. A fiber optic couples the light to the photomultiplier tube (PMT), where it is recorded by a Brookhaven Instruments BI-9000 correlator. Upon the onset of micelle formation at pH^* and α^* the scattered intensity significantly increases. Certain regions of the intensity versus α curves

are linear, allowing extrapolation to the baseline to obtain α^* . As seen in the Figure 4, α^* increases with the ionic strength due to screening of electrostatic repulsions, allowing micelles to form at higher fractional charge α . In our studies of the micelle structure, we remain below the α^* curves in Figure 4 such that we observe the charge and ionic strength dependence without inducing micelle breakup.

3.4 Dynamic Light Scattering

Dynamic light scattering (DLS) measurements were performed as described in more detail elsewhere.⁴² Data were collected over a duration ranging from 4 min to 30 min, and the data was stored and processed on a Brookhaven Instruments BI-9000 correlator. In converting from an intensity autocorrelation to an electric field correlation, the correlator calculates the baseline $\langle I(t) \rangle^2$ and also measures the baseline at long delay times τ . The measured and calculated baselines are typically within 0.2% for our copolymer/micelle solutions. For dilute, monodisperse particles the autocorrelation function $g^{(1)}(\mathbf{q}, \tau)$ is an exponential decay $g^{(1)}(\mathbf{q}, \tau) = e^{-q^2 D_o \tau}$ where the self diffusion coefficient D_o is related to the particle hydrodynamic size R_h and viscosity μ by the Stokes Einstein equation $D_o = \frac{k_B T}{6\pi\mu R_h}$.

For a system with a distribution of sizes the autocorrelation function $g^{(1)}(\mathbf{q}, \tau)$ takes the form⁵⁷

$$g^{(1)}(\mathbf{q}, \tau) = \int_0^\infty F(R_h) \exp \left[-\frac{q^2 k_B T}{6\pi\mu} R_h^{-1} \tau \right] dR_h + \Delta \quad (14)$$

with a distribution of exponential decays. Scattering from large impurities such as dust contributes to the autocorrelation function as an additive “dust term” Δ . The filtered samples were generally dust free, and the dust term was usually well below 0.01 or it was disregarded.

The autocorrelation data was analyzed using CONTIN,⁵⁸ a FORTRAN program producing an optimum $F(R_h)$ size distribution via a constrained Laplace transform of the data. The optimum smoothing to fit the data called for a ‘probability to reject’ of 0.4. We report the average of 3-5 measurements at a 90° scattering angle; individual measurements at other scattering angles confirmed these results.

Shown in Figure 5 are representative CONTIN distributions for each of the copolymer micelles, where the experimental results shown by the markers are averages over five repeated measurements. The solid lines in Figure 5 are Schulz distribution⁵⁹ fits of the distributions yielding fractional standard deviations of 0.26, 0.30, and 0.37 for the DMAEMA–DEAEMA, PEO–DEAEMA, and Q-DMAEMA–DEAEMA micelles, respectively.

3.5 Small Angle Neutron Scattering

We performed small angle neutron scattering (SANS) measurements at the National Institute of Standards and Technology (NIST) Center for Neutron Research (NCNR) in Gaithersburg, MD. Measurements were taken at the 8 m SANS instrument on beamline NG1 as well as on the 30 m instrument on beamline NG3. A 6 m detector distance with a 25.0 cm detector offset from the beam center and a wavelength $\lambda = 6 \text{ \AA}$ on the 30 m instrument provided an accessible scattering vector q range of $0.008 < q < 0.11 \text{ \AA}^{-1}$. On the 8 m beamline a sample to detector distance of 3.6 m, 3.5° detection angle and incident wavelengths of 5 and 9 Å gave q values spanning $0.008 < q < 0.19 \text{ \AA}^{-1}$. Sample cells of 1 mm path length were used. The scattering profiles were corrected for background and empty cell scattering, and effects from solvent scattering were accounted for by subtracting data from salt solutions of various

concentrations in D₂O from that of the corresponding copolymer solutions.

Homopolymer and copolymer micelle solutions were prepared as described above, using D₂O (Isotec) as the solvent and titrating with DCl and KOD (Aldrich). Complementary DLS experiments were performed on these same deuterated samples to measure micelle hydrodynamic radii.

We obtain R_g for both the micelles and homopolymers from a Guinier analysis, using

$$I(q) = I(0)e^{-q^2R_g^2/3} \quad (15)$$

Representative Guinier plots are shown in Figure 6 for the DMAEMA–DEAEMA micelles at 0.001 g/ml. Homopolymer radii of gyration are also obtained by fitting the homopolymer scattering profile with the Debye equation⁶⁰ for the scattering from isolated random coils

$$I(q) = I(0) \left(\frac{2}{x^2} \right) (x - 1 + e^{-x}) \quad (16)$$

Here $x = (qR_g)^2$, and the Debye equation gives R_g values which we find from our measurements to be generally $\sim 25\%$ larger than those obtained from the Guinier equation. Representative homopolymer Guinier and Debye fits are shown in Figure 7.

From the y intercept of fits to the micelle SANS Guinier plots, we compare $I(0)$ the micelle scattered intensity at $q = 0$, to that of a homopolymer of known molecular weight.⁴² We estimate the micelle aggregation numbers f through the ratio of intensities for the homopolymer and micelles given by the Zimm equation, assuming low concentrations such that the second virial term is negligible, resulting in

$$\frac{M_{w,m}}{M_{w,h}} = \left(\frac{c_h}{c_m} \right) \left(\frac{\rho_h^N - \rho_o^N}{\rho_{bcp}^N - \rho_o^N} \right)^2 \left(\frac{\rho_{bcp}}{\rho_h} \right)^2 \left(\frac{I(0)_m}{I(0)_h} \right) \quad (17)$$

The subscripts m , bcp and h correspond to micelle, block copolymer and homopolymer, respectively. Estimates of the scattering length densities ρ^N were calculated by summing over the scattering lengths of the atoms in each molecule⁶¹ and are tabulated in Table 4.

The properties of the homopolymers used to estimate f , including PEO, DMAEMA, Q-DMAEMA, and bet-DMAEMA are tabulated in Table 3. The different homopolymers gave slightly different values for the aggregation number for a given micelle solution, and the reported aggregation numbers are averages over f obtained using different homopolymers.

The intermediate scattering region in the SANS scattering profile at higher q values provides information about the degree of swelling in the micelle corona, through the Flory exponent ν . The scattering profile approaches an $I(q) \sim q^{1/\nu}$ scaling in the intermediate scattering region, and the data can be fit to obtain ν . The scattering profile can also be plotted in the form of a Kratky plot, as shown in Figure 8 for representative DMAEMA–DEAEMA scattering profiles. In the figure, at $\alpha = 0.37$ the corona is swollen, where the positive slope where the line is fitted represents $\nu > 1/2$. Conversely, at $\alpha = 0.19$ the corona is shrunken as indicated by the the negative slope showing $\nu < 1/2$.

There have been studies in the literature where the entire scattering profile is fit to a model form factor.^{62–69} We are unable to fit a large portion of our scattering profiles to a simple core-shell model.⁶⁵ Contrast matching experiments where the core and corona are observed separately may make this possible.

4 Results - pH Dependent Measurements

4.1 Weakly Charged Corona: DMAEMA–DEAEMA

We adjust the fractional charge α in the micelle corona by changing the solution pH and calculate α , knowing the amount of acid and base added. One important parameter which varies with α is the DMAEMA statistical segment length a . SANS measurements of the DMAEMA homopolymer R_g provide estimates of a as a function of α . The homopolymer coil is expected to take on an approximately Gaussian density profile, with $R_g = \sqrt{Na^2/6}$. Using this expression for R_g and the constraint that Na equals the polymer contour length, we calculate the number of statistical segments N and a from Guinier and Debye fits to SANS measurements. A power-law fit through the data for a versus α in Figure 9 gives the dependence $a \sim \alpha^{0.2}$. From the constraint that Na equals the contour length $N \sim \alpha^{-0.2}$.

We measure R_h , R_g , f , and ν as a function of the solution pH. We present these measurements in terms of the fractional charge α in Figure 10 for 0.005 g/ml copolymer concentrations, where the effective amount of KCl added during the titrations amounts to 0.03 M. Also included in Figure 10a are R_h measurements obtained for 0.001 g/ml copolymer solutions, with 0.006 M effective KCl added from titrations.

As seen in Figure 10a the micelle hydrodynamic size R_h for the 0.001 g/ml solutions are larger for solutions with larger α due to the swelling of the corona from electrostatic repulsions. The swelling in the corona at higher α can also be observed in Figure 10d, where the Flory exponent ν increases with increasing α ; however, in the 0.005 g/ml solution, R_h decreases with increasing α for $\alpha < 0.24$. An explanation can be found upon observation of the reduction in micelle aggregation number f with charge α in Figure 10c. As the

electrostatic repulsions are increased at higher α , fewer copolymer chains aggregate, forming smaller micelles. Hence the slight decrease in R_h with increasing α for $\alpha < 0.24$ reflects the decrease in f with α . In general, increasing the fractional charge α decreases the aggregation number while at the same time swelling the corona, and these two offsetting effects on the overall micelle size lead to a subtle α dependence on R_h .

The curve through the aggregation number data in Figure 10c comes from a power-law fit from which the scaling $f \sim \alpha^{-1.5}$ is obtained. As described earlier Khokhlov and coworkers²³ predict a scaling for the aggregation number described in Equation 10. Substituting the $N_s \sim \alpha^{-0.2}$ and $a \sim \alpha^{0.2}$ dependences into Equation 10 gives the overall α dependence $f \sim \alpha^{-1.2}$, which is similar to the measured $\alpha^{-1.5}$ scaling.

As seen in Figure 10b R_g decreases with increasing α , reflecting its strong dependence on the micelle core. If we assume no solvent swelling in the core, the micelle core size varies as $f^{1/3}$, and so the decrease in R_g with increasing α reflects the decrease in f in Figure 10c.

From the data, we calculate the ratio R_g/R_h as a function of α . The R_g/R_h ratio provides a picture of the degree of swelling in the micelle corona, where low R_g/R_h indicates a swollen corona, due to the fact that R_g is more heavily weighted by the micelle core and R_h increases more rapidly with increased coronal swelling. As seen in Figure 11 R_g/R_h decreases with increasing α , in accord with the earlier discussion that the corona swells as the fractional charge increases. The R_g/R_h ratio for a solid sphere is well known⁷⁰ to be $\sqrt{3/5} \sim 0.77$, and the lower micelle R_g/R_h ratios in Figure 11 are expected, due to the presence of a dense micelle core. Munk and coworkers⁷¹ have shown R_g/R_h for individual micelles to be around 0.4.

In Figure 10d ν decreases below 0.5 at low α , indicating sub- Θ solvent conditions. This

apparent sub- Θ scaling in the corona may reflect the interesting molecular structure of these polyacrylate amines.⁷² The association between amine and carbonyl groups may cause cyclization with one monomer⁷² or intrachain interactions that would appear as an effective segmental attraction.

4.2 Electrostatically Neutral Corona: PEO–DEAEMA

PEO–DEAEMA block copolymers contain the electrostatically neutral PEO block which is not expected to depend on α , allowing the study of the α dependence of the DEAEMA core independently of that of the corona. As shown in Figure 12 the PEO–DEAEMA micelle R_h decreases with increasing α due to a decrease in the aggregation number caused by repulsions between core blocks, which was seen for the DMAEMA–DEAEMA micelles in Figure 10c. Since the PEO corona is not sensitive to α the competing tendency of the corona to swell with increasing α is absent.

4.3 Comparison with Theoretical Models

From the data in Figure 10 the corona thickness L is calculated by subtracting the overall micelle radius R_h from the core radius R_c . R_c is calculated from the measured aggregation numbers in Figure 10c, assuming that the DEAEMA blocks form a densely packed core with a density equal to that of bulk DEAEMA. From R_c and f the grafting density σ can also be calculated. From the $f \sim \alpha^{1.5}$ dependence found from the experimental measurements we calculate the scalings $R_c \sim \alpha^{-0.5}$ and $\sigma \sim \alpha^{-0.5}$. The measured L dependence on α is compared to that predicted by theoretical models from the literature in order to gain ad-

ditional insight into the nature of the charging. Shown in Figure 13 are corona thicknesses L , with a power law fit, giving the scaling $L \sim \alpha^{0.28}$. As described earlier the osmotic and salted regimes correspond to low and high salt concentrations, respectively. The amount of salt added during micelle preparation amounts to 0.03 M, while the counterion concentration ranges from 0.043 to 0.073 M depending on α , suggesting that the micelle corona is somewhere between the osmotic and salted regimes. Closer examination of the data in Figure 13 suggests two different α scalings, where the data fitted for $\alpha > 0.2$ as shown by the dashed line gives the exponent 0.41.

As described more in detail in the Theory section, polyelectrolyte brushes are considered in two limits: quenched brushes, where the positions of the charges are fixed on the chains, and the annealed brush, where they vary along the contour lengths of the polymer chains. Summarized in Table 5 are scaling relations for L , assuming $L \sim \alpha^m$. The scaling exponent m describes the direct dependence on α without considering the dependence of a , N , R_c and σ with varying α . We know that the segment size increases with charge as $a \sim \alpha^{0.2}$ and the number of statistical segment decreases as $N \sim \alpha^{-0.2}$ as shown in Figure 9. As described earlier R_c scales as $\alpha^{-0.5}$ while σ scales as $\alpha^{-0.5}$. These scalings of a and σ with α can be substituted into the expressions from the model which describe L as a function of a , σ , and α to give an overall scaling exponent m^* such that $L \sim \alpha^{m^*}$. The m^* values obtained by including the a and σ scalings are included in the last column of Table 5. The analytical self-consistent-field (SCF) model of Leermakers and coworkers²⁹ for the annealed osmotic brush does not have the simple power law scaling on α ; however, a power law fit to a log-log plot of Equation 11 within the experimental α range of $0.15 < \alpha < 0.37$ gives the effective m , listed in Table 5.

The models in Table 5 generally overpredict m^* , with a stronger α dependence than that seen experimentally. The SCF model for annealed brushes at a planar interface give particularly stronger α dependences. Typically, $R_c \sim 10$ nm and $R_h \sim 30$ nm, such that models for a curved interface are more appropriate. The MF models describing the quenched osmotic brush^{23,26–28} give $m^* \sim 0.5$, in reasonable agreement with the data. The MF model of Zhulina and Borisov²⁶ for the annealed osmotic brush at a spherical interface might be expected to better describe the DMAEMA–DEAEMA micelles. The model, as seen in Equation 13 does not give a direct α dependence, and in Table 5 $m = 0$. Due to the a , N , R_c and σ dependences alone, $m^* \sim 1.7$, giving a much stronger α dependence than the data show. The model also describes an internal sublayer within a radius R_n in the corona where the chains behave like a neutral brush. Due to the a , N , R_c and σ dependences the neutral brush thickness for a curved interface, described by Equation 6, gives $m^* \sim -0.28$. The negative value of m^* indicates that the inner layer shrinks with increasing α . The neutral internal sublayer in addition to the outer annealed charged layer gives the total coronal thickness. A large internal sublayer might be expected because the fractional charge α is relatively low at $\sim 15 - 40\%$, and the opposing effects of the inner and outer layers combined could cause the overall m^* to approach that measured experimentally. Hence from comparison of the data with the models we infer a picture for the DMAEMA–DEAEMA micelles which looks similar to the cartoons of Figures 2b and 2c.

5 Results - Dependence on Ionic Strength

5.1 Weakly Charged Corona: DMAEMA–DEAEMA

The ionic strength dependence of the DMAEMA–DEAEMA micelle hydrodynamic radius R_h , radius of gyration R_g , and aggregation number f are shown in Figures 14 and 15. Results from 0.001 and 0.005 g/ml copolymer concentrations are shown, with the dependence on salt added before micellization in Figure 14 and salt added after micellization in Figure 15. Small amounts of salt are inevitably formed during titration; the effective amount added in these experiments is 0.006 and 0.03 M KCl for the 0.001 and 0.005 g/ml copolymer concentrations, respectively. The ordinate of the graphs in Figures 14 and 15 accounts for this in the total salt concentration. The DMAEMA–DEAEMA copolymers were titrated to form micelles at constant fractional charges α of 0.17 and 0.2 for the 0.001 and 0.005 g/ml solutions, respectively.

As seen in Figure 14a when salt is added prior to the formation of micelles, R_h remains relatively constant; however, as shown in Figure 15a, when salt is added after micelle formation, R_h decreases with the addition of salt. We expect the addition of salt to screen the electrostatic repulsions in the charged corona, leading to a smaller corona thickness, as observed in the decrease in R_h when salt is added after the formation of micelles. Prior to micellization, both blocks of the copolymers are highly charged, thus electrostatic repulsions work against the formation of micelles during the titrations. Addition of salt before micellization screens the electrostatic repulsions, allowing larger numbers of chains to aggregate to form larger micelles during the titrations. This increase in the aggregation number f is seen in Figure 14c. Hence when added prior to the formation of micelles, the salt tends to

cause larger micelles to form, while at the same time shrinking the micelle corona. These two offsetting effects cause the weak dependence of R_h .

Measurements of the DMAEMA–DEAEMA radius of gyration R_g are shown as a function of added salt in Figures 14b and 15b. When salt is added after micellization, R_g decreases with added salt, following the same trend as the decrease in R_h . When salt is added before micellization, we find that R_g increases with added salt, in contrast with the weak R_h dependence. The competing effects of the increasing aggregation number and the decrease in the corona thickness have opposite effects on the micelle size, but since R_g is more heavily weighted toward the micelle core it more directly reflects the increased aggregation number in Figure 14c.

Aggregation numbers for DMAEMA–DEAEMA micelles are plotted in Figures 14c and 15c for salt added before and after micellization. As discussed above, adding salt before micellization screen electrostatic repulsions between chains allowing the formation of larger numbers of chains to come together to form micelles with larger f . When salt is added after micelle formation, the aggregation number is relatively constant, as seen in Figure 15c.

The difference in R_h , R_g and f depending on the order of salt addition suggests that the micelles are non-equilibrium structures. Micelle formation and breakup upon addition of base or acid occurs extremely quickly, on the time scale of milliseconds. The fast micellization kinetics may impede equilibration. The deviation in the R_h , R_g , and f behavior persists even weeks after sample preparation, suggesting that rearrangement of chains between micelles is extremely slow due to strong hydrophobic attractions in the micelle core.

5.2 Electrostatically Neutral Corona: PEO–DEAEMA

The PEO–DEAEMA copolymer allows us to study the effect of ionic strength on the core DEAEMA block separately. The R_h , R_g and f dependence on salt are shown in Figure 16, at the concentrations and conditions described in the figure caption. The copolymers were titrated with sufficient base such that the DEAEMA core $\alpha = 0$.

Because the PEO block is electrostatically neutral, electrostatic screening in the corona is probably not responsible for the salt dependent behavior. As seen in Figure 16a, when salt is added after micelle formation, the decrease in R_h seen for DMAEMA–DEAEMA is absent because of the electrostatically neutral PEO corona. When salt is added prior to titration, R_h increases with added salt since the salt screens the electrostatic repulsions between DEAEMA blocks, allowing larger numbers of copolymers to aggregate into the core of larger micelles. The competing effect of the salt causing the DMAEMA corona to shrink is absent in the PEO corona, such that the PEO–DEAEMA R_h reflects the increase in f .

The R_g data for PEO–DEAEMA micelles shown in Figure 16b follow the same trend for salt added before micellization as seen in DMAEMA–DEAEMA micelles. For salt added after micellization, R_g does not decrease since, in contrast to the DMAEMA–DEAEMA micelles, the PEO micelle corona is uncharged.

PEO–DEAEMA aggregation numbers shown in Figure 19c support the R_h and R_g results. When salt is added prior to micellization, the aggregation number increases due to electrostatic screening of the core forming DEAEMA blocks. When salt is added after micellization, the aggregation number remains relatively constant.

5.3 Highly Charged Corona: Q-DMAEMA–DEAEMA

We study the dependence of the Q-DMAEMA–DEAEMA copolymer on ionic strength, where the micelle corona is a strong polyelectrolyte. The copolymers are titrated such that $\alpha \sim 0$ for the DEAEMA block to form micelles. The Q-DMAEMA block forming the micelle corona remains fully charged at $\alpha \sim 1$ and is independent of the solution pH.

In these micelles, R_h increases with ionic strength, whether salt is added prior to or after micellization, as seen in Figure 17a. This behavior contrasts with the DMAEMA–DEAEMA and the PEO–DEAEMA behavior, and the difference is expected to be caused by the highly charged Q-DMAEMA corona. As salt is added and screens the electrostatic repulsions, additional unimers are incorporated into the micelles to increase their size.

We find that the apparent aggregation numbers of the Q-DMAEMA–DEAEMA micelles increase with added salt, whether salt is added before or after micellization, as seen in Figure 17c. The smaller and highly charged micelles are able to rearrange even when salt is added after micellization, such that the dependence on f is the same in both cases.

The trends for R_g with ionic strength follow those in R_h , as seen in Figure 17. The trends are similar whether salt is added prior to or after micellization. As R_g favors the core radius, the increase of R_g with salt reflects the increase in aggregation number.

5.4 Comparison with Theoretical Models

5.4.1 Star-like Micelle Model

We start by examining the star-like micelle model for predictions of R_h and R_g with varying f for the simplest case of electrostatically neutral micelles. As described earlier, SANS

experiments were performed on DMAEMA, Q-DMAEMA, and PEO homopolymers to obtain the statistical segment a in the micelle corona. For the DMAEMA homopolymer, an average a at $\alpha \sim 0.2$ was used to match the conditions where the DMAEMA–DEAEMA micelle R_g and R_h were measured. From a we calculate volume per segment V_s and the number of segments N_s per chain in the corona. The core DEAEMA block is considered to be densely packed and thus the definition of the statistical segment in the micelle core is irrelevant. NMR studies have indicated dehydration of the micelle core,⁷³ so the core density, ρ_c comes directly from the DEAEMA core monomer molecular weight and density. Using SANS Kratky plots as a guide, 0.5 and 0.6 were used for the Flory exponent ν for DMAEMA and PEO, respectively. We use these parameters summarized in Table 6 to calculate R_c , R_g , and R_m from the star-like micelle model. The SANS neutron scattering length densities ρ^N used in the model to calculate R_g are tabulated in Table 4.

The experimentally measured PEO–DEAEMA R_h and R_g data from Figure 16 are plotted in Figure 18 as a function of the aggregation number f , along with curves predicted by the star-like model. We find excellent quantitative agreement between the data and the model, and the R_g/R_h values of ~ 0.55 for the data are comparable to the values of ~ 0.6 from the model.

The DMAEMA–DEAEMA R_h and R_g data from Figures 14 and 15 do not agree well with predictions from the star-like model, as shown in Figure 19. Also included in Figure 19 are Q-DMAEMA–DEAEMA data from Figure 17. Quantitatively, R_g is somewhat under-predicted by the model, while R_h is greatly underpredicted. The closer agreement between the measured and predicted R_g values indicates that the model does well in predicting the core size, which is more heavily weighted in R_g . The disagreement between the model and

experimental results is not surprising, as the model was developed for neutral micelles. The charges in the micelle corona alter the blob picture in the corona, such that the model is inadequate to describe the DMAEMA–DEAEMA R_g and R_h behavior.

The disagreement between the DMAEMA–DEAEMA data and the star-like micelle model motivates us to incorporate the concept of the ‘electrostatic blob’. Khokhlov and coworkers,²³ as well as Borisov²² describe an electrostatic blob as presented in the Theory section where the number of segments per blob N_ξ is constrained such that the energy from the electrostatic repulsions between two adjacent blobs equals the thermal energy $k_B T$. This definition of the electrostatic blob applies for micelles with low aggregation numbers and low salt where few of the counterions remain in the corona such that Coulombic interactions are important. The crossover between the inner region of the corona where neutral blobs are close packed and the outer region where the blobs are electrostatic is calculated to be the point where the neutral blob size equals the electrostatic blob size. However, for the DMAEMA–DEAEMA micelles where $f \sim 200$ and $R_m \sim 30$ nm the crossover region for this electrostatic blob model occurs outside of the micelle corona thickness, such that all of the blobs are close packed.

Borisov²² as well as Zhulina and Borisov²⁶ also describe a different electrostatic blob occurring at large aggregation numbers where most of the counterions remain in the corona and dominate the swelling. In this case the blob size is constrained such that there is one charge in each blob, so that the number of segments per blob N_ξ is α^{-1} . These electrostatic blobs are each of the same size, as depicted in Figure 2b. Describing the blobs to exhibit the Flory scaling $\xi = N_\xi^\nu a$ the electrostatic blob size becomes $\xi_e = \alpha^{-\nu} a$ and the corona

thickness is simply the sum of αN blobs

$$L = \alpha^{1-\nu} Na \tag{18}$$

For $\nu = 1/2$, equation 18 is the same Equation 5, and the blob analysis shows that the constant of proportionality for the scaling in Equation 5 is approximately 1. Through this analysis we demonstrate that Equation 5 can be quantitatively compared with the experimental data. We find from the parameters of our DMAEMA–DEAEMA micelles that the crossover between non-electrostatic and electrostatic blobs occurs within the micelle core, such that all of the blobs in the corona are electrostatic. We can add the predicted corona thickness with the predicted core radius from the star-like micelle model to obtain a model for the overall micelle size R_m

$$R_m = \left(\frac{3N_c f}{4\pi\rho_c} \right)^{1/3} + \alpha^{1/2} Na \tag{19}$$

for $\nu = 1/2$.

We obtain a density profile of polymer segments for a corona containing electrostatic blobs as $\rho_e = \alpha^{\nu-1} f/4\pi ar^2$ which can be integrated to determine R_g . Shown in Figure 19 are predictions of R_m and R_g from the electrostatic blob model. As seen in Figure 19, this fairly simple model does well in describing the data and predicts $R_g/R_h \sim 0.55$. This is a significant improvement from the star-like micelle model, despite the fact that the electrostatic blob model does not account for annealing in the micelle corona.

5.4.2 Models for Salt Dependence of Polyelectrolyte Brushes

The micelle corona thickness L is calculated as $R_h - R_c$, as described earlier. The models of Birshtein and coworkers,²⁸ as well as Leermakers and coworkers²⁹ predict L to scale as

$\sigma^{1/3}C_s^{-1/3}$, while Tirrell and coworkers^{20,21} developed a model in which $L \sim \sigma^{1/3}C_s^{-2/3}$. In addition, the model of Russel and coworkers gives the scaling $L \sim \sigma^{1/3}C_s^{-1/6}$ for a brush at a planar interface and for a highly curved interface $L \sim \sigma^{1/5}R_c^{2/5}C_s^{-1/10}$. To separate the salt dependence of σ and R_c , we plot $L/\sigma^{1/3}$ and $L/\sigma^{1/5}R_c^{2/5}$ against C_s in Figure 20a and b. As seen in Figure 20, above a certain ionic strength the data qualitatively agrees with, yet is unable to distinguish between the $\sigma^{1/3}C_s^{-1/3}$, $\sigma^{1/3}C_s^{-1/6}$ and $\sigma^{1/5}R_c^{2/5}C_s^{-1/10}$ scalings. The corona thickness is nearly constant at low ionic strengths and the data exhibits a crossover in the ionic strength dependence at a salt concentration of approximately 0.05 M. A similar type of behavior was seen by Russel and coworkers²⁵ where a nearly constant micelle size is observed at low ionic strengths and the scaling behavior seen at salt concentrations greater than 10^{-4} M.

We explain the crossover at low ionic strengths by examining the Debye screening length κ^{-1} and the counterion concentration within the corona. Shown in Figure 21a is the same data in Figure 20 with the salt concentration expressed in the form κ^{-1}/ξ in the bottom ordinate axis. As described earlier $\kappa \sim C_s^{1/2}$ and the Debye screening length κ^{-1} represents the length scale over which electrostatic repulsions are important. With ξ_e defined as the electrostatic blob size $\kappa^{-1}/\xi_e > 1$ corresponds to ionic strengths where the Debye screening length κ^{-1} is greater than the electrostatic blob size ξ_e . With $\kappa^{-1} > \xi_e$ electrostatic repulsions between blobs are virtually unscreened, such that further increases in the Debye screening length by reduction of the ionic strength has little effect on the corona thickness.

In addition, the micelle corona contains counterions balancing the coronal charge. The ordinate axis in Figure 21b shows the total salt concentration C_s normalized by the counterion concentration C_{count} . At $C_s/C_{count} < 1$ the salt concentration decreases below the

counterion concentration, and at $C_s \ll C_{count}$ the electrostatic screening due to the added salt is negligible relative to that of the counterions, leading to the nearly constant corona thickness with added salt. As seen in Figure 21b the crossover occurs near $C_s/C_{count} \sim 1$, demonstrating the importance of the counterions in the structure of the micelle corona.

6 Conclusions

Dynamic light scattering and small angle neutron scattering were used to characterize the structural properties of polyelectrolyte micelles with varying fractional charge α and ionic strength. Two opposing effects on the overall micelle size are the aggregation number f and the degree of swelling in the micelle corona. Increasing α tends to decrease f and increase the coronal swelling, due to the increase in electrostatic repulsions, while increasing the ionic strength has the opposite effect on f and the swelling due to electrostatic screening. Both effects are seen in the DMAEMA–DEAEMA micelles, due to the pH sensitive α in both the core and coronal blocks. Studies of the PEO–DEAEMA micelles illustrate the effect of charge and salt on the core block only, and the micelle structure is found to be governed by f , without the effect of the coronal swelling. The highly charged Q-DMAEMA–DEAEMA micelles follow the salt dependence of DMAEMA–DEAEMA micelles, except that the Q-DMAEMA–DEAEMA micelles are able to rearrange after the formation of micelles, due to their high charge and small size. We compare the experimental data to theoretical models and find that the DMAEMA–DEAEMA weakly charged micelle corona can be described by an electrostatic blob picture.

7 Acknowledgements

This work was supported by the Center for Polymer Interfaces and Macromolecular Assemblies through the National Science Foundation MRSEC program (DMR 9808677). J.A.P. and A.P.G. acknowledge the support of the Stanford Synchrotron Radiation Laboratory through the Department of Energy Contract DE-AC03-76SF00515. We acknowledge the support of the National Institute of Standards and Technology, US Department of Commerce for providing the facilities used in the neutron scattering experiments described in this paper.

References

- [1] Tuzar, Z. and Kratochvil, P., *Adv. Colloid Interface Sci.* **1976** 6, 201.
- [2] Halperin, A., Tirrell, M., and Lodge, T. P., *Advances in Polymer Science* **1992** 100, 31.
- [3] Zhang, L. and Eisenberg, A., *Science* **1995** 268, 1728.
- [4] Zhang, L., Yu, K., and Eisenberg, A., *Science* **1996** 272, 1777.
- [5] Gast, A. P., *Langmuir* **1996** 12, 4060.
- [6] Vagberg, L. J. M., Cogan, K. A., and Gast, A. P., *Macromolecules* **1991** 24, 1670.
- [7] Cogan, K. A. and Gast, A. P., *Macromolecules* **1991** 24, 6512.
- [8] Cogan, K. A. and Gast, A. P., *Macromolecules* **1990** 23, 745.
- [9] Farinha, J. P. S., d'Oliveira, J. M. R., Martinho, J. M. G., Xu, R., and Winnik, M. A., *Langmuir* **1998** 14, 2291.
- [10] Cogan, K. A., Leermakers, F. A. M., and Gast, A. P., *Langmuir* **1992** 8, 429.
- [11] Daoud, M. and Cotton, J. P., *Journal de Physique (Paris)* **1982** 43, 531.
- [12] Noolandi, J. and Hong, K. M., *Macromolecules* **1983** 16, 1443.
- [13] Marques, C., Joanny, J. F., and Leibler, L., *Macromolecules* **1988** 21, 1051.
- [14] Dan, N. and Tirrell, M., *Macromolecules* **1992** 25, 2890.
- [15] Wijmans, C. M. and Zhulina, E. B., *Macromolecules* **1993** 26, 7214.

- [16] Grest, G. S., Kremer, K., and Witten, T. A., *Macromolecules* **1987** *20*, 1376.
- [17] Witten, T. A. and Pincus, P. A., *Macromolecules* **1986** *19*, 2509.
- [18] Misra, S., Varanasi, S., and Varanasi, P. P., *Macromolecules* **1989** *22*, 4173.
- [19] Pincus, P., *Macromolecules* **1991** *24*, 2912.
- [20] Argillier, J. F. and Tirrell, M., *Theoretica Chimica Acta* **1992** *82*, 343.
- [21] Dan, N. and Tirrell, M., *Macromolecules* **1993** *26*, 4310.
- [22] Borisov, O. V., *Journal de Physique II* **1996** *6*, 1.
- [23] Shusharina, N. P., Nyrkova, I. A., and Khokhlov, A. R., *Macromolecules* **1996** *29*, 3167.
- [24] Biver, C., Hariharan, R., Mays, J., and Russel, W. B., *Macromolecules* **1997** *30*, 1787.
- [25] Hariharan, R., Biver, C., Mays, J., and Russel, W. B., *Macromolecules* **1998** *31*, 7506.
- [26] Zhulina, E. B. and Borisov, O. V., *Macromolecules* **1996** *29*, 2618.
- [27] Israëls, R., Leermakers, F. A. M., and Fleer, G. J., *Macromolecules* **1994** *27*, 3087.
- [28] Zhulina, E. B., Birshtein, T. M., and Borisov, O. V., *Macromolecules* **1995** *28*, 1491.
- [29] Lyatskaya, Y. V., Leermakers, F. A. M., Fleer, G. J., Zhulina, E. B., and Birshtein, T. M., *Macromolecules* **1995** *28*, 3562.
- [30] Szczubialka, K., Ishikawa, K., and Morishima, Y., *Langmuir* **1999** *15*, 454.
- [31] Procházka, K., Martin, T. J., Munk, P., and Webber, S. E., *Macromolecules* **1996** *29*, 6518.

- [32] Guenoun, P., Davis, H. T., Tirrell, M., and Mays, J. W., *Macromolecules* **1996** *29*, 3965.
- [33] Baines, F. L., Armes, S. P., Billingham, N. C., and Tuzar, Z., *Macromolecules* **1996** *29*, 8151.
- [34] Guenoun, P., Schlachli, A., Sentenac, D., Mays, J. W., and Benattar, J. J., *Physical Review Letters* **1995** *74*, 3628.
- [35] An, S. W., Thirtle, P. N., Thomas, R. K., Baines, F. L., Billingham, N. C., Armes, S. P., and Penfold, J., *Macromolecules* **1999** *32*, 2731.
- [36] van der Maarel, J. R. C., Groenewegen, W., Egelhaaf, S. U., and Lapp, A., *Langmuir* **2000** *16*, 7510.
- [37] Baines, F. L., Billingham, N. C., and Armes, S. P., *Macromolecules* **1996** *29*, 3416.
- [38] Biesalski, M., Rühle, J., and Johannsmann, D., *Journal of Chemical Physics* **1999** *111*, 7029:7037.
- [39] Groenewegen, W., Egelhaaf, S. U., Lapp, A., and van der Maarel, J. R. C., *Macromolecules* **2000** *33*, 3283.
- [40] Groenewegen, W., Lapp, A., Egelhaaf, S. U., and van der Maarel, J. R. C., *Macromolecules* **2000** *33*, 4080.
- [41] Martin, T. J., Procházka, K., Munk, P., and Webber, S. E., *Macromolecules* **1996** *29*, 6071.

- [42] Lee, A. S., Bütün, V., Armes, S. P., and Gast, A. P., *Macromolecules* **1999** *32*, 4302.
- [43] Selb, J. and Gallot, Y., Ionic Block Copolymers, in *Developments in Block Copolymers - 2*, edited by Goodman, I., pages 27–96, Elsevier Applied Science Publishers, New York, 1985.
- [44] Yatvin, M. B., Kreutz, W., Horwitz, B. A., and Shinitzky, M., *Science* **1980** *210*, 1253.
- [45] Seki, K. and Tirrell, D. A., *Macromolecules* **1984** *17*, 1692.
- [46] Thomas, J. L. and Tirrell, D. A., *Accounts of Chemical Research* **1992** *25*, 336.
- [47] Mosler, R. and Hatton, T. A., *Current Opinion in Colloid and Interface Science* **1996** *1*, 540.
- [48] Bütün, V., Billingham, N. C., and Armes, S. P., *Chemical Communications* **1997** , 671.
- [49] Vamvakaki, M., Billingham, N. C., and Armes, S. P., *Macromolecules* **1999** *32*, 2088.
- [50] Lowe, A. B., Billingham, N. C., and Armes, S. P., *Chemical Communications* **1996** , 1555.
- [51] Bütün, V., Bennett, C. E., Vamvakaki, M., Lowe, A., Billingham, N. C., and Armes, S. P., *Journal of Materials Chemistry* **1997** *7*, 1693.
- [52] Wesley, R. D., Cosgrove, T., Thompson, L., Armes, S. P., Billingham, N. C., and Baines, F. L., *Langmuir* **2000** *16*, 4467.
- [53] Milner, S. T., Witten, T. A., and Cates, M. E., *Macromolecules* **1988** *21*, 2610.

- [54] Odijk, T. and Houwaart, A. C., *Journal of Polymer Science: Polymer Physics Edition* **1978** *16*, 627.
- [55] Fixman, M., *Journal of Physical Chemistry* **1990** *15*, 6283.
- [56] Oxtoby, D. W. and Nachtrieb, N. H., *Principles of Modern Chemistry*, Saunders College Publishing, Philadelphia, 1986.
- [57] Provencher, S. W., Hendrix, J., DeMaeyer, L., and Paulussen, N., *Journal of Chemical Physics* **1978** *69*, 4273.
- [58] Provencher, S. W., *Computer Physics Communications* **1982** *27*, 213.
- [59] Bartlett, P. and Ottewill, R. H., *Journal of Physical Chemistry* **1992** *96*, 3306.
- [60] Debye, P., *Journal of Physical and Colloidal Chemistry* **1947** *51*, 18.
- [61] Higgins, J. S. and Maconnachie, A., Neutron Scattering from Macromolecules in Solution, in *Polymers in Solution*, edited by Forsman, W. C., pages 183–238, Plenum Press, New York, 1986.
- [62] Dozier, W. D., Huang, J. S., and Fetters, L. J., *Macromolecules* **1991** *24*, 2810.
- [63] Stellbrink, J., Willner, L., Jucknischke, O., Richter, D., Lindner, P., Fetters, L. J., and Huang, J. S., *Macromolecules* **1998** *31*, 4189.
- [64] Pedersen, J. S., Egelhaaf, S. U., and Schurtenberger, P., *Journal of Physical Chemistry* **1995** *99*, 1299.

- [65] Poppe, A., Willner, L., Allgaier, J., Stellbrink, J., and Richter, D., *Macromolecules* **1997** *30*, 7462.
- [66] Nakano, M., Matsuoka, H., Yamaoka, H., Poppe, A., and Richter, D., *Macromolecules* **1999** *32*, 697.
- [67] Schurtenberger, P., Jerke, G., Cavaco, C., and Pedersen, J. S., *Langmuir* **1996** *12*, 2433.
- [68] Jerke, G., Pedersen, J. S., Egelhaaf, S. U., and Schurtenberger, P., *Langmuir* **1998** *14*, 6013.
- [69] Won, Y.-Y., Davis, H. T., and Bates, F. S., *Science* **1999** *283*, 960.
- [70] Mallamace, F. and Micali, N., Low Angle Light Scattering and its Applications, in *Light Scattering: Principles and Development*, edited by Brown, W., pages 381–438, Clarendon Press, Oxford, 1996.
- [71] Qin, A., Tian, M., Ramireddy, C., Webber, S. E., Munk, P., and Tuzar, Z., *Macromolecules* **1994** *27*, 120.
- [72] Příkladný, M. and Ševčík, S., *Makromolekulare Chemie* **1985** *186*, 111.
- [73] Bütün, V., PhD thesis, University of Sussex, 1999.

8 Tables

Investigators	Predicted Thickness L	Geometry	Salt
Ionic Strength Dependences			
Argillier and Tirrell ²⁰	$L \sim N(a^2\sigma)^{1/3}C_s^{-2/3}$	Plane	Salted
Dan and Tirrell ²¹	$L \sim aN_s^{3/5}f^{1/5}/\phi_s^{2/5}$	Sphere	Salted
Russel, Odijk, Fixman, <i>et al.</i> ^{25,54,55}	$L \sim \sigma^{1/3}C_s^{-1/2}$	Plane	Salted
Russel, <i>et al.</i> ²⁵	$L \sim \sigma^{1/3}C_s^{-1/6}$	Plane	Salted
Russel, <i>et al.</i> ²⁵	$L \sim R_c^{2/5}\sigma^{1/5}C_s^{-1/10}$	Sphere	Salted
Pincus ¹⁹	$L \sim Na\sigma^{1/3}(aC_s)^{-1/3}$	Plane	Salted
Fractional Charge α Dependences			
Pincus, ¹⁹ Zhulina, <i>et al.</i> ²⁶	$L \sim \alpha^{1/2}Na$	Sphere/Plane	Osmotic
Khokhlov, <i>et al.</i> ²³	$L \sim N_s(l_b/a)^{2/7}\alpha^{4/7}a$	Sphere	Osmotic
Neutral Brush			
Zhulina, <i>et al.</i> ²⁶	$L \sim N^{1/2}a(R_c^2\sigma)^{1/4}$	Sphere	–

Table 1: Summary of model predictions: Quenched Brushes.

Investigators	Predicted Thickness L	Geometry	Salt
Birshtein, <i>et al.</i> ²⁸	$L \sim Na^{4/3}\sigma^{-1/3} \left(\frac{\alpha_b}{1-\alpha_b}(C_H^* + C_s) \right)^{1/3}$	Plane	Osmotic
Birshtein, <i>et al.</i> ²⁸	$L \sim N(a^2\alpha^2\sigma C_s^{-1})^{1/3}$	Plane	Salted
Leermakers, <i>et al.</i> ²⁹	$L \sim Na\sqrt{-\ln(1 - \alpha_b) - \alpha_o}$	Plane	Osmotic
Leermakers, <i>et al.</i> ²⁹	$L \sim Na \left(\frac{2}{\pi^2}\sigma \frac{\alpha_b^2}{\Phi^+} \right)^{1/3}$	Plane	Salted
Zhulina, <i>et al.</i> ²⁶	$L \sim aN_s^3(Ka^3)/\sigma R_c^2$	Sphere	Osmotic

Table 2: Summary of model predictions: Annealed Brushes

Sample	Molecular Weight	M_w/M_n	A units	B units
DMAEMA-DEAEMA	32,600	1.10	97	94
PEO-DEAEMA	8,300	1.33	45	34
Q-DMAEMA-DEAEMA	44,900		97	94
DEAEMA homopolymer	15,000	1.06	–	81
DMAEMA homopolymer	12,300	1.08	78	–
PEO homopolymer	1,470	1.05	33	–
bet-DMAEMA homopolymer	22,350	1.14	80	–

Table 3: Copolymer and homopolymer properties

Molecule	$\rho^N \times 10^{-9} \text{ (cm}^2\text{)}$
DMAEMA	8.1
PEO	6.4
Q-DMAEMA	11.5
DEAEMA	5.6
DMAEMA-DEAEMA	6.9
PEO-DEAEMA	6.1
Q-DMAEMA-DEAEMA	8.6
D ₂ O (ρ_o^N)	63.7

Table 4: SANS scattering length densities ρ^N

Investigators	Model	m	m^*
Results from Experiments			0.28 (0.41)
Quenched Osmotic Brush			
Zhulina, <i>et al.</i> , ²⁶			
Israëls, <i>et al.</i> , ²⁷			
Birshtein, <i>et al.</i> , ²⁸	MF (planar+spherical)	1/2	1/2
Khokhlov, <i>et al.</i> , ²³	MF (spherical)	4/7	0.51
Annealed Osmotic Brush			
Leermakers, <i>et al.</i> , ²⁹	Analytical SCF (planar)	0.58	0.58
Zhulina, <i>et al.</i> , ²⁶	MF (spherical)	0	1.7
Annealed Salted Brush			
Leermakers, <i>et al.</i> , ²⁹	Analytical SCF (planar)	2/3	2/3
Neutral Brush			
Zhulina, <i>et al.</i> , ²⁶	MF (spherical)	0	-0.28

Table 5: Model predictions for corona thickness with varying fractional charge

Copolymer	a (nm)	V_s (nm ³)	ρ_c (nm ⁻³)	ν	N_c	N_s
DMAEMA-DEAEMA	1.2	0.69	3.41	0.5	94	26
PEO-DEAEMA	0.61	0.09	3.41	0.6	34	33

Table 6: Parameters used in the star-like micelle model

9 Figure Captions

Figure 1. Chemical structures of novel pH sensitive copolymers.

Figure 2. Cartoons of the (a) star-like micelle, (b) micelle with a charged quenched corona, and (c) micelle with a charged annealed corona.

Figure 3. Titration curves for DMAEMA–DEAEMA (\circ), PEO–DEAEMA (\square), and Q-DMAEMA–DEAEMA (\triangle) copolymers. Lines are model calculations.

Figure 4. Critical fractional charge α^* for micelle formation with varying salt concentration. Values are shown for 0.001 g/ml (\square) and 0.005 g/ml (\circ) DMAEMA–DEAEMA and 0.001 g/ml PEO–DEAEMA (\triangle) copolymers. Also shown is a measurement for 0.004 g/ml Q-DMAEMA–DEAEMA (\diamond). Lines are interpolations to guide the eye.

Figure 5. Representative DLS CONTIN size distributions for DMAEMA–DEAEMA (\circ), PEO–DEAEMA (\square), and Q-DMAEMA–DEAEMA (\triangle) micelles. Lines are fits to a theoretical Schulz distribution to obtain polydispersities.

Figure 6. Representative Guinier plots for DMAEMA–DEAEMA micelles at 0.006M (\circ), 0.046M (\square), and 0.086M (\triangle) salt concentrations.

Figure 7. Representative Guinier (upper) and Debye (lower) fits for 0.01 g/ml DMAEMA homopolymer solution with $\alpha = 0.2$. The same scattering profile is shown twice with that of the Debye fit offset in the negative direction for clarity.

Figure 8. Representative SANS scattering Kratky plots for 0.005 g/ml DMAEMA–

DEAEMA micelle solutions for $\alpha = 0.37$ (\circ) and $\alpha = 0.19$ (\square). Lines are fits used to obtain values of the Flory exponent ν .

Figure 9. Statistical segment length a with varying α . The best fit to data (—) gives $a \sim \alpha^{0.2}$.

Figure 10. R_h , R_g , f , and ν measurements of DMAEMA–DEAEMA micelles with varying α . Measurements were made for 0.001 g/ml (\diamond) and 0.005 g/ml (\circ) copolymer solutions. The line in (c) is a power law fit, and the line in (d) is an interpolation to guide the eye. The ionic strength is nearly constant for each copolymer concentration. Error bars for R_h and R_g are generally within the size of the markers.

Figure 11. R_g/R_h for DMAEMA–DEAEMA micelles with varying α . Lower values of R_g/R_h indicate swelling of the micelle corona.

Figure 12. R_h for 0.001 g/ml PEO–DEAEMA micelles with varying α .

Figure 13. Experimentally measured coronal layer thickness L with varying fractional charge α . Fits to all the data (—) and for $\alpha > 0.2$ (- - -) give $m^* = 0.28$ and 0.41, respectively.

Figure 14. DMAEMA–DEAEMA micelle hydrodynamic radius R_h , radius of gyration R_g and aggregation number f as a function of salt added before micellization, at 0.001 g/ml (filled) and 0.005 g/ml (open) copolymer concentrations. $\alpha \sim 0.17$ and 0.20 for the 0.001 g/ml and 0.005 g/ml solutions, respectively. Error bars for R_h and R_g are generally within the size of the markers.

Figure 15. DMAEMA–DEAEMA micelle hydrodynamic radius R_h , radius of gyration R_g and aggregation number f as a function of salt added after micellization, at 0.001 g/ml (filled) and 0.005 g/ml (open) copolymer concentrations. $\alpha \sim 0.17$ and 0.20 for the 0.001 g/ml and 0.005 g/ml solutions, respectively. Error bars for R_h and R_g are generally within the size of the markers.

Figure 16. PEO–DEAEMA hydrodynamic radius R_h , radius of gyration R_g and aggregation number f vs. ionic strength data for salt added before (\circ) and after (\square) micellization at 0.001 g/ml for R_h and 0.01 g/ml for R_g and f measurements. Micelles at 0.005 g/ml (\triangle) were also studied. $\alpha = 0$ for all solutions. Error bars for R_h and R_g are generally within the size of the markers.

Figure 17. Q-DMAEMA–DEAEMA hydrodynamic radius R_h , radius of gyration R_g and aggregation number f vs. ionic strength data for salt added before (\circ) and after (\square) micellization. The data are for 0.005 g/ml solutions, with $\alpha = 0$ in the DEAEMA blocks. Error bars for R_h and R_g are generally within the size of the markers.

Figure 18. Experimentally measured R_h (\bullet) and R_g (\circ) as a function of f for PEO–DEAEMA micelles. Results are compared with the star-like micelle model which predicts R_c (—), R_g (- - -), and R_h ($\cdot\cdot\cdot$).

Figure 19. Experimental R_h (filled) and R_g (open) measurements as a function of f for 0.001 g/ml (\circ), 0.005 g/ml (\square), and 0.0075 g/ml (\triangle) DMAEMA–DEAEMA micelle solutions. Also included are results for Q-DMAEMA–DEAEMA micelles (\diamond). Results are compared with the star-like micelle model which predicts R_c (—), R_g (- - - -), and R_h (- - -), as well as for

the electrostatic blob model for R_g (- - -) and R_h (\cdots).

Figure 20. (a) $L/\sigma^{1/3}$ scaling for a planar interface. (b) $L/\sigma^{1/5}R_C^{2/5}$ scaling for a highly curved interface. Shown in (a) are $C_s^{1/3}$ (- - -) and $C_s^{1/6}$ (—) scalings, and in (b) $C_s^{1/10}$ (—).

The scalings are multiplied by an arbitrary constant to overlay the data.

Figure 21. (a) $L/\sigma^{1/3}$ scaling with κ^{-1}/ξ_e (b) $L/\sigma^{1/3}$ scaling with C_s/C_{count} . Shown in (a) are $(\kappa^{-1})^{2/3}$ (- - -) and $(\kappa^{-1})^{1/3}$ (—) scalings, and in (b) $C_s^{-1/3}$ (- - -) and $C_s^{-1/6}$ (—). The

scalings are multiplied by an arbitrary constant to overlay the data.

10 Figures

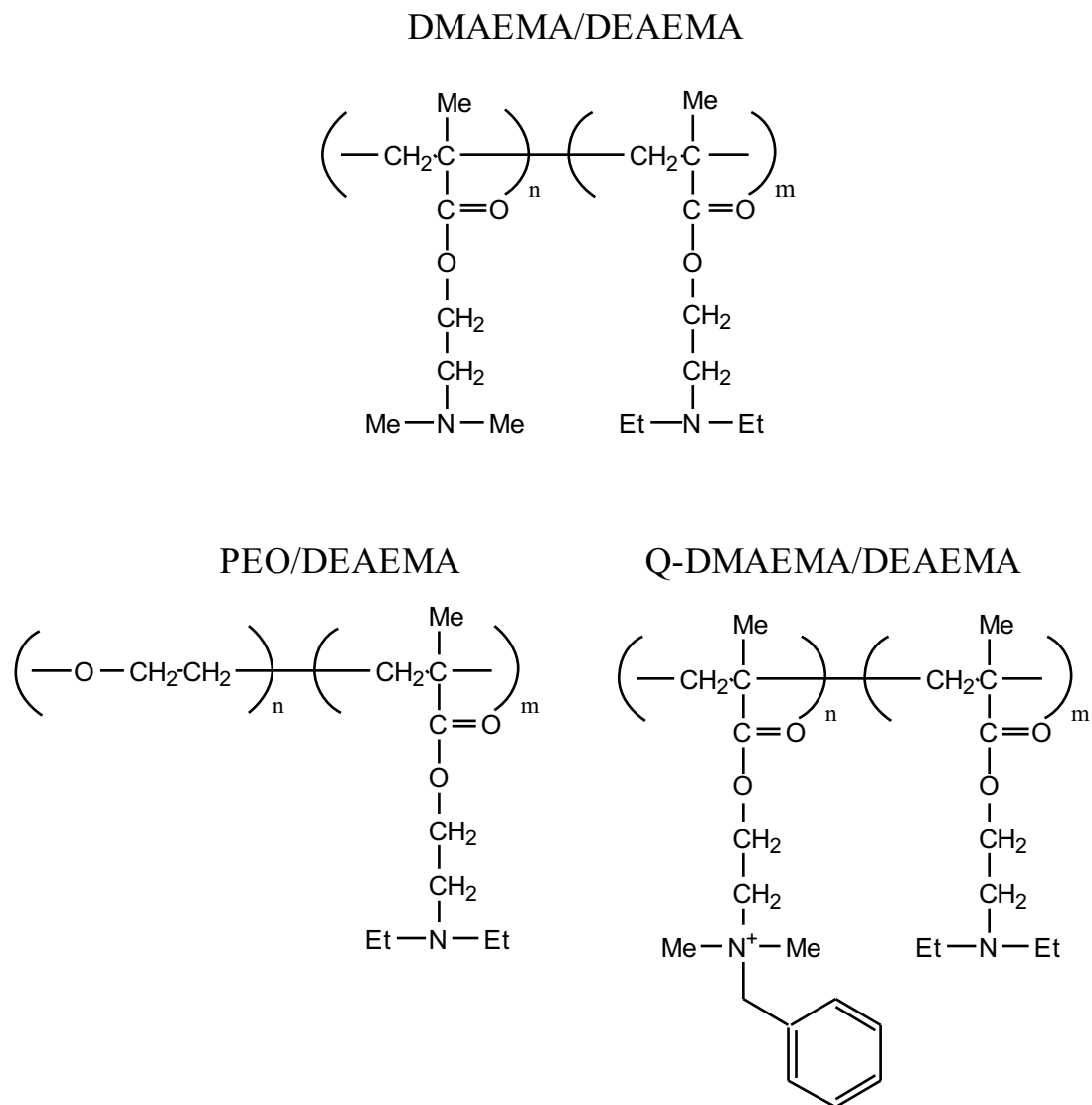


Figure 1.

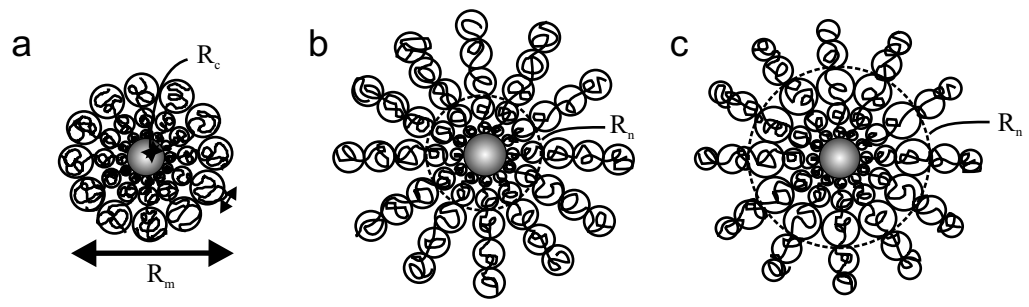


Figure 2.

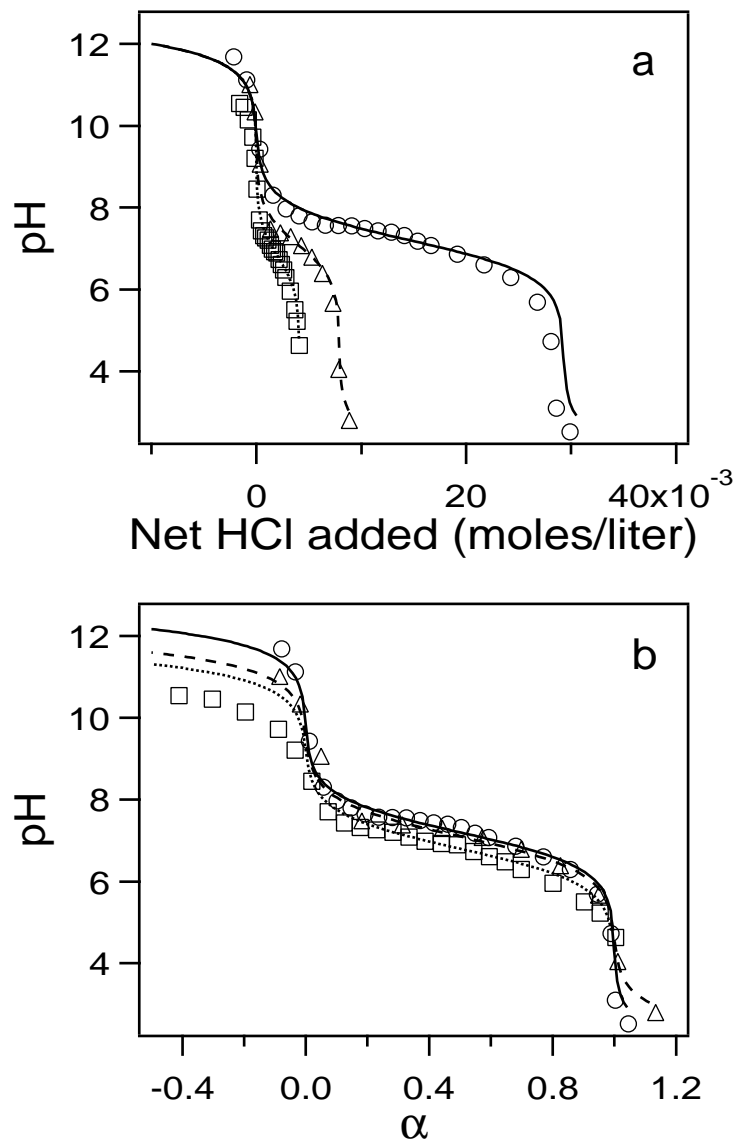


Figure 3.

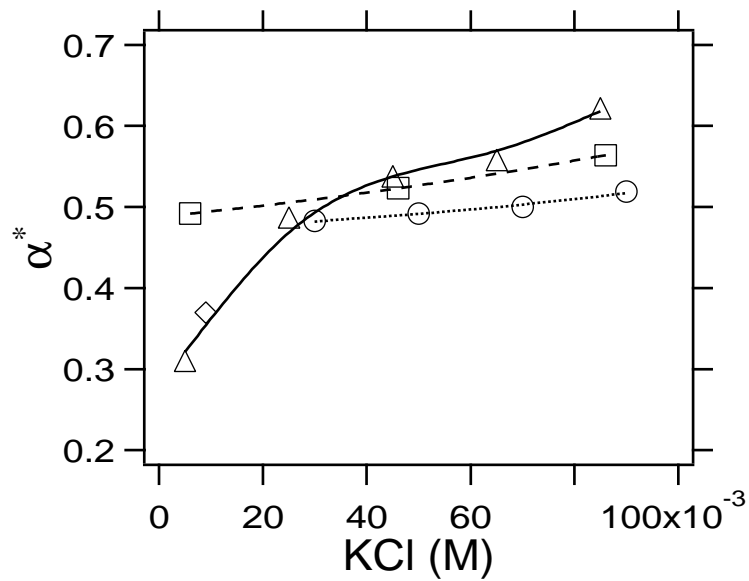


Figure 4.

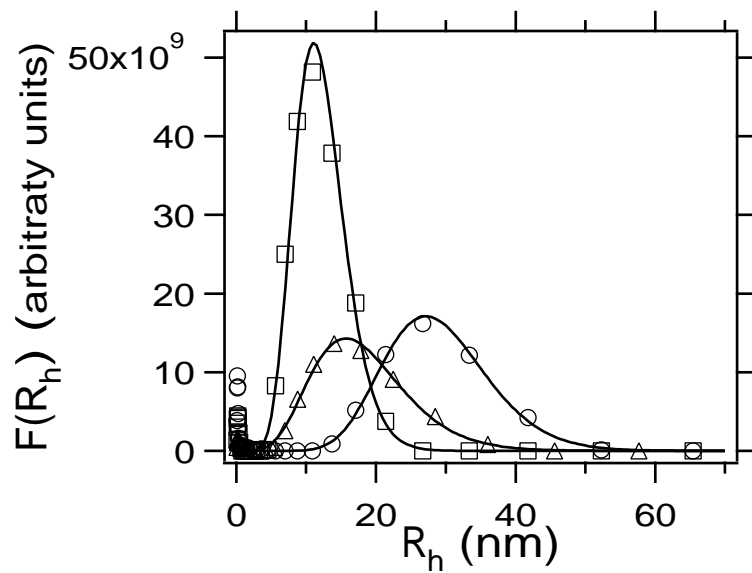


Figure 5.

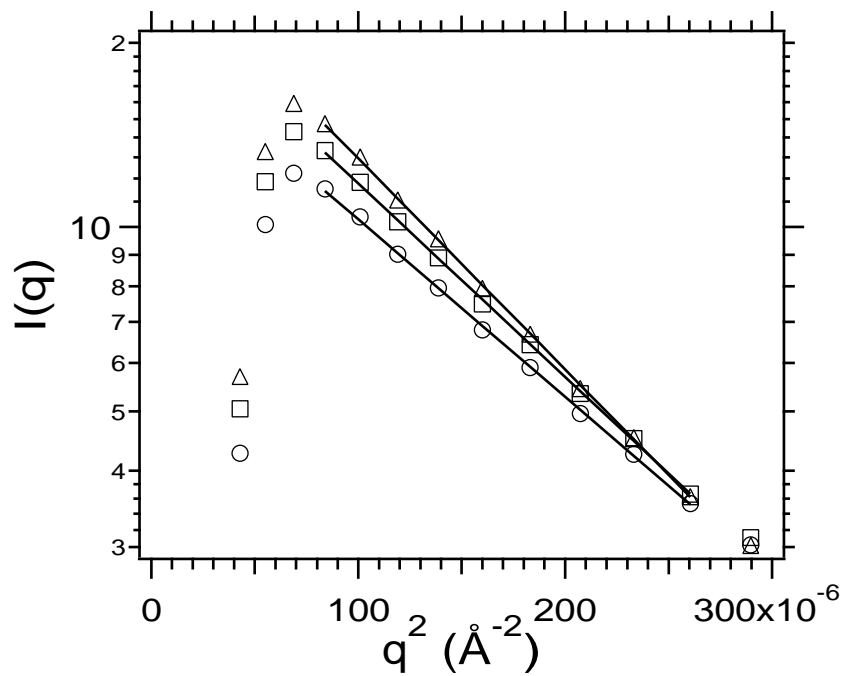


Figure 6.

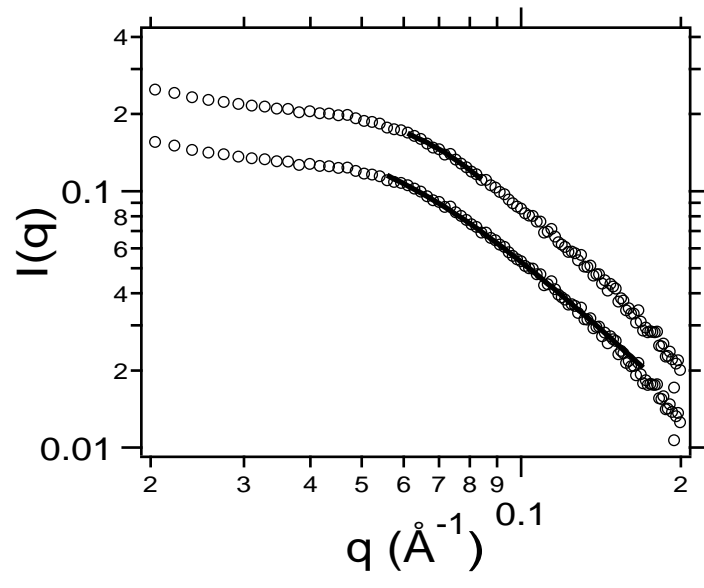


Figure 7.

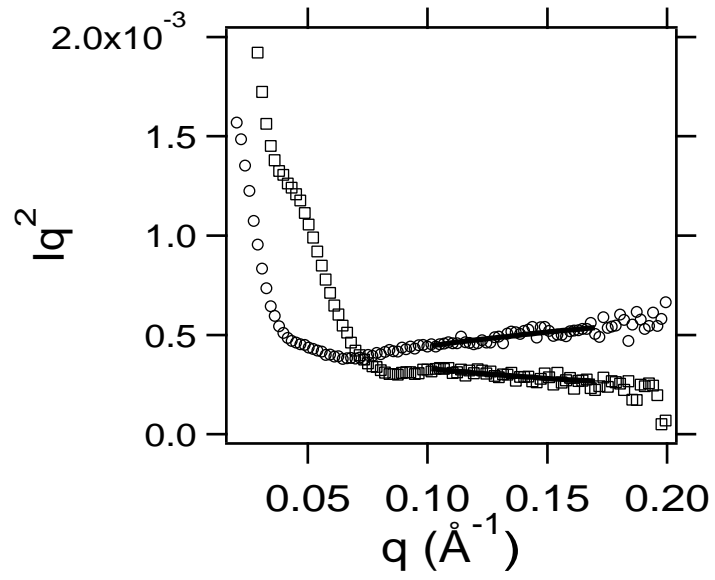


Figure 8.

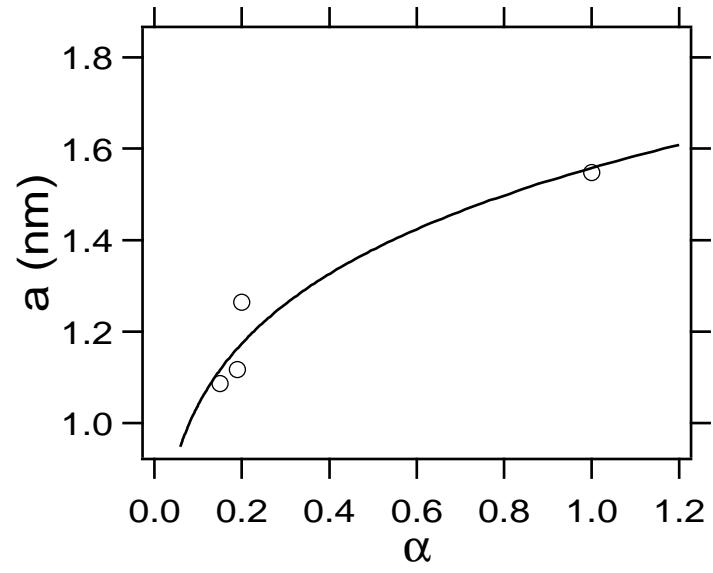


Figure 9.

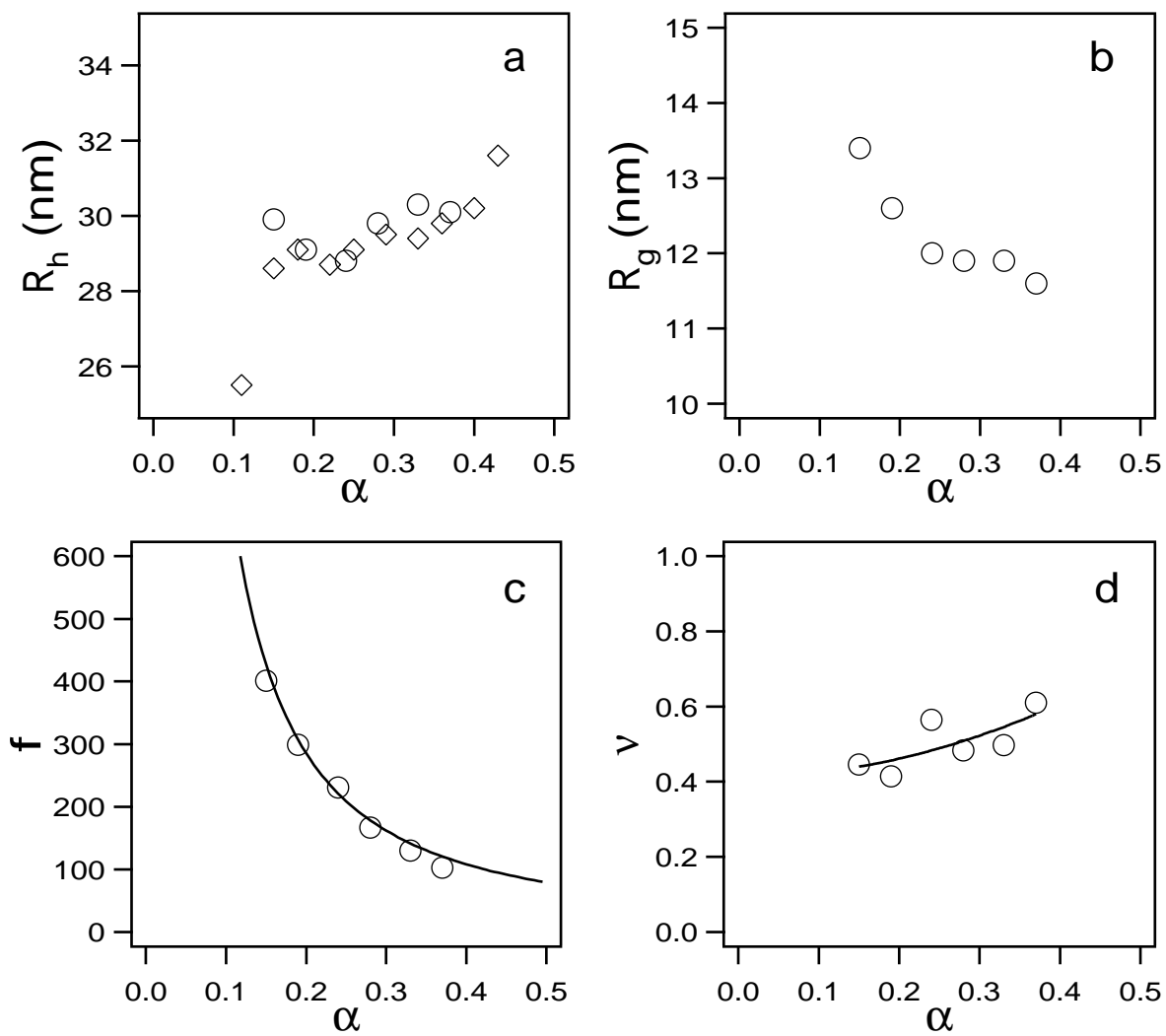


Figure 10.

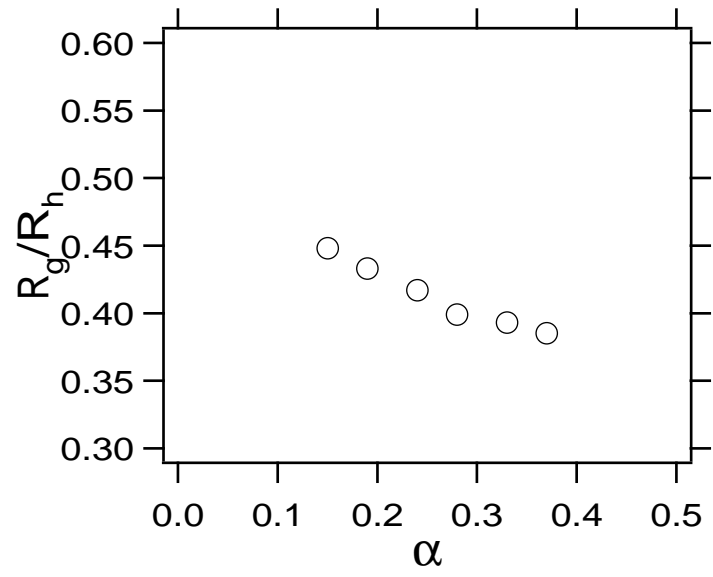


Figure 11.

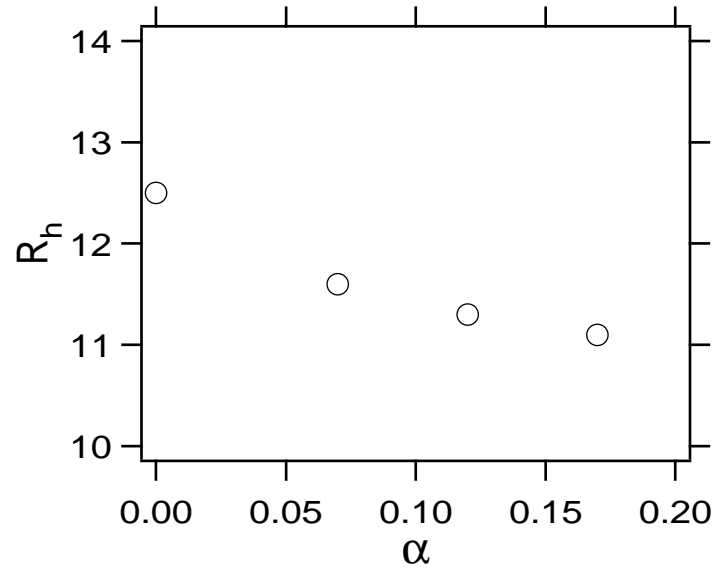


Figure 12.

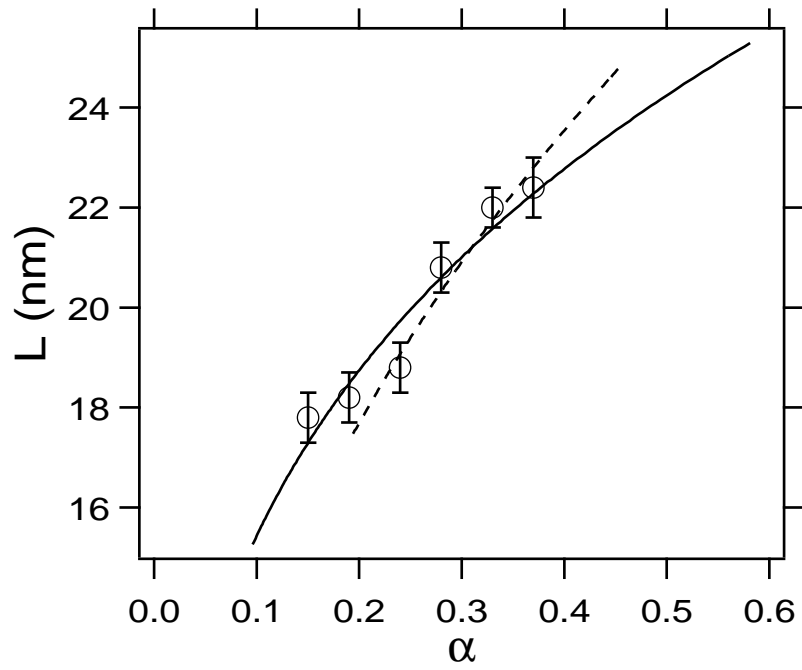


Figure 13.

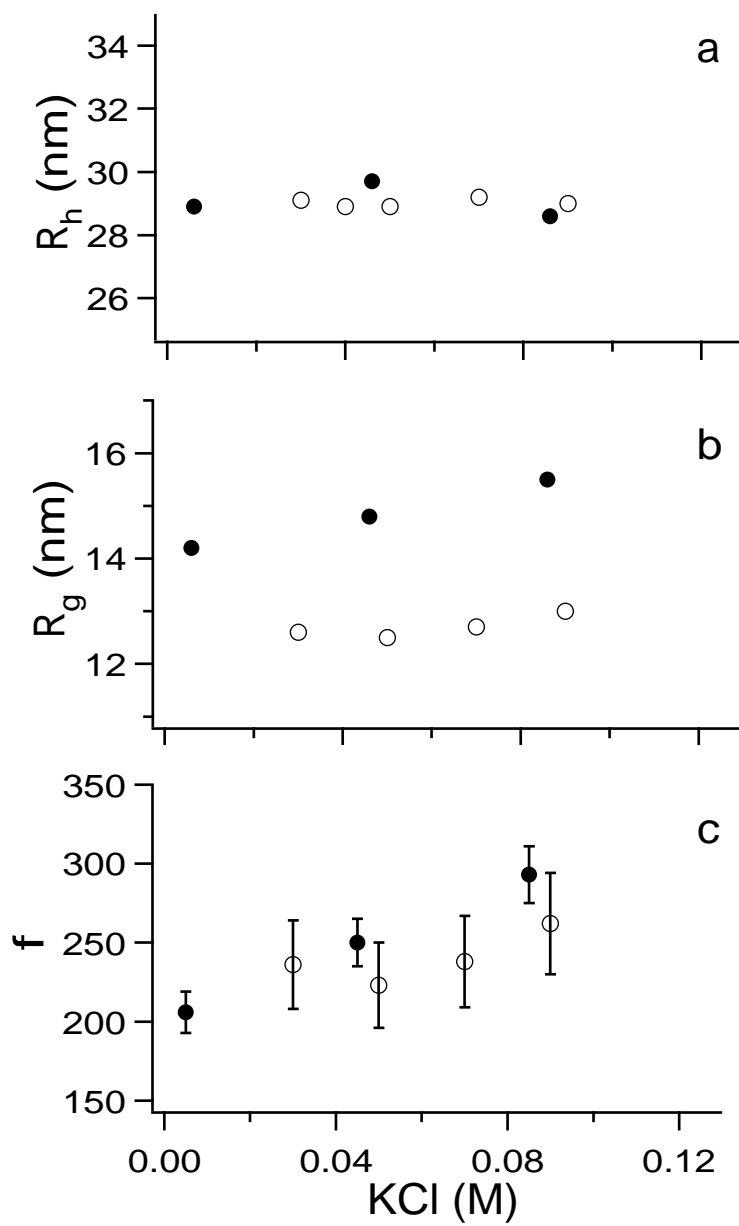


Figure 14.

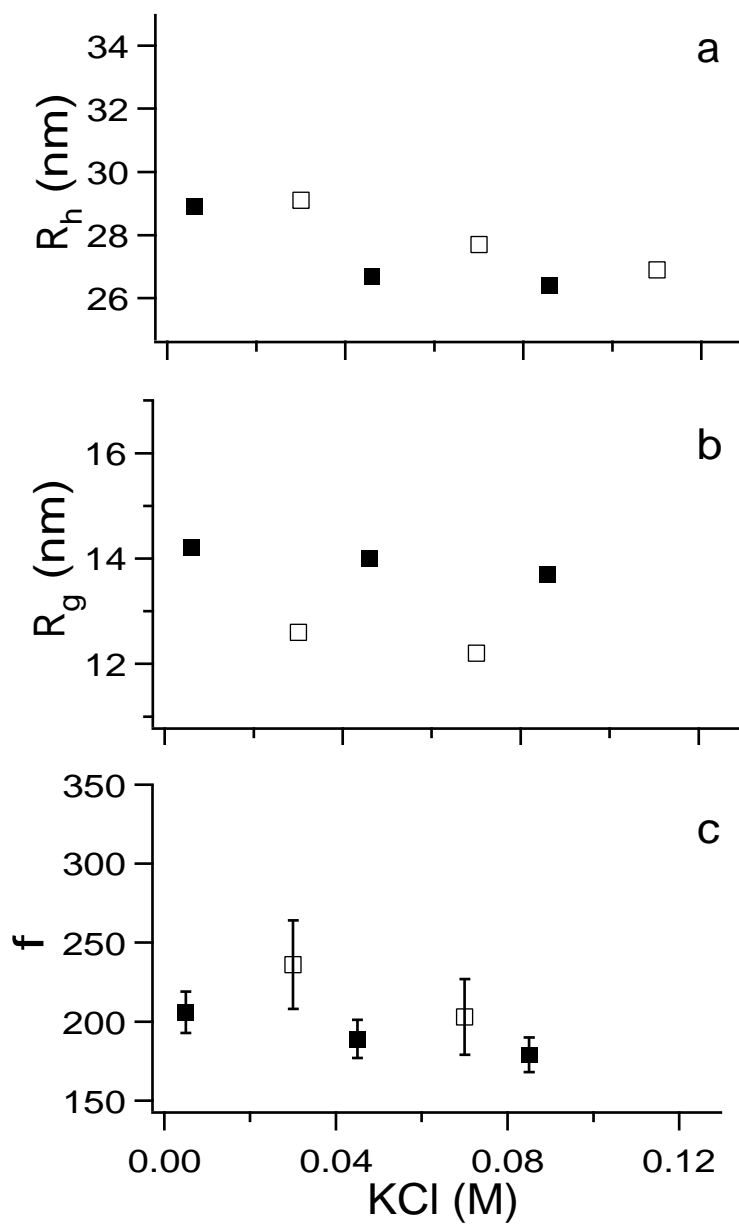


Figure 15.

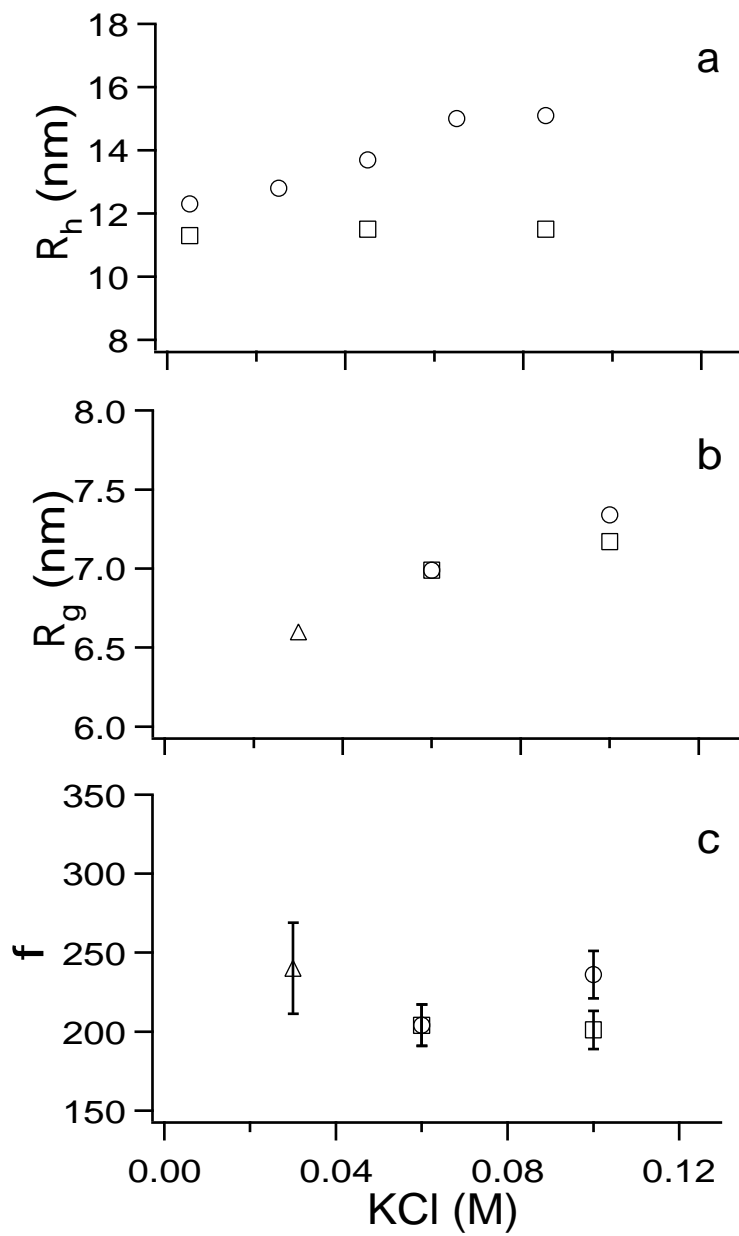


Figure 16.

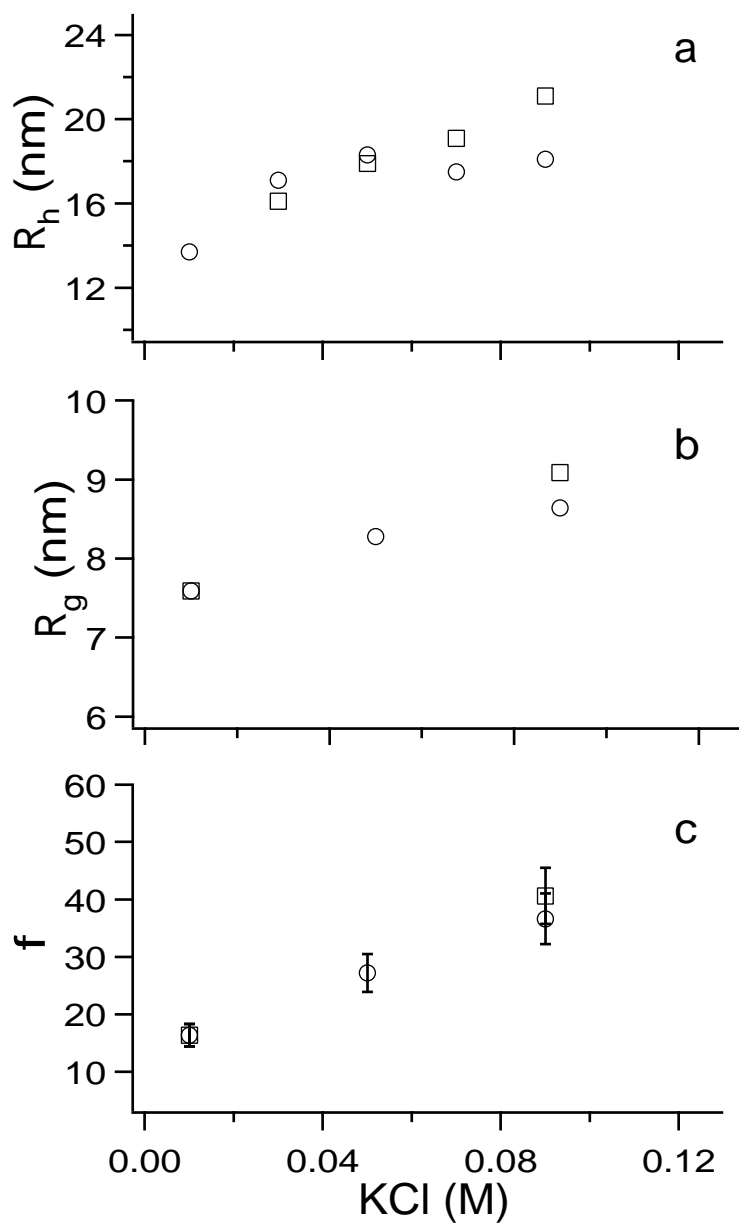


Figure 17.

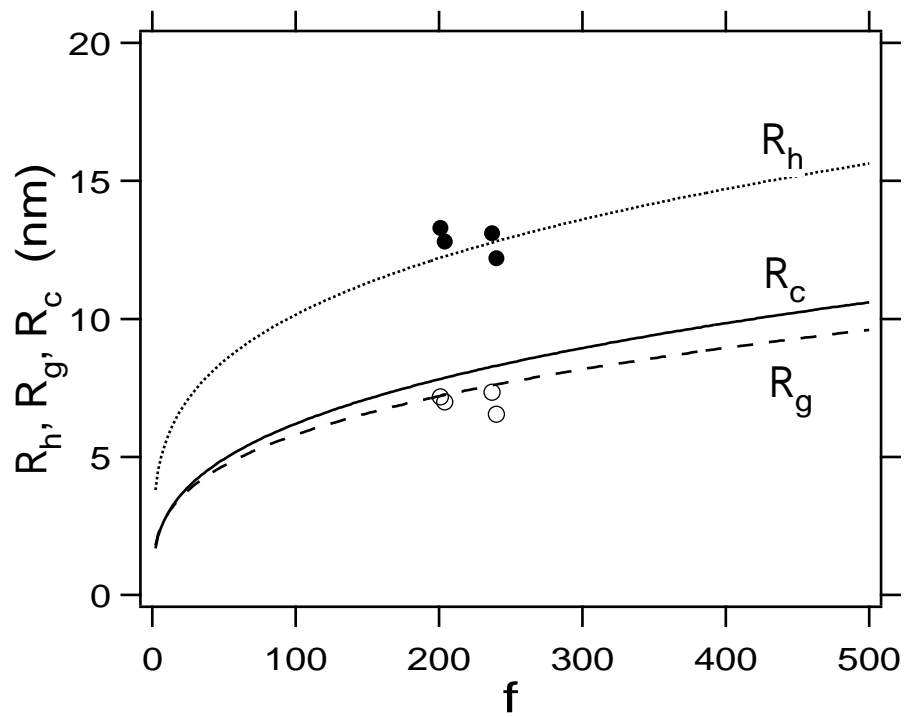


Figure 18.

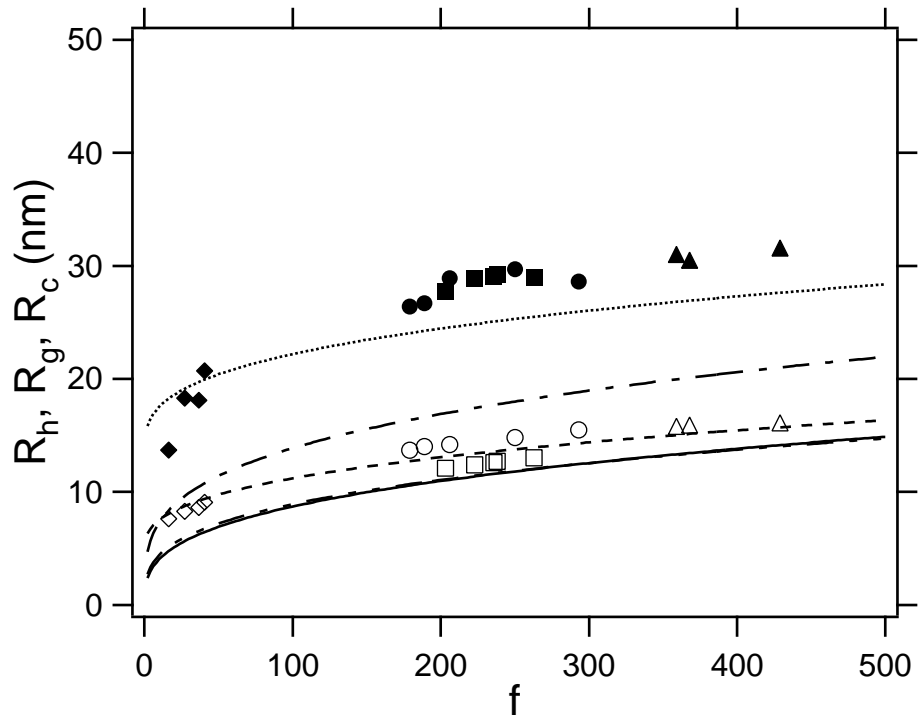


Figure 19.

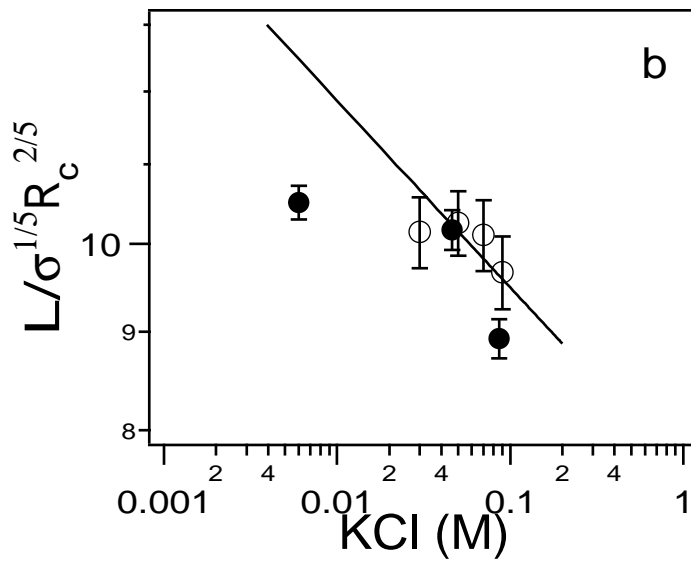
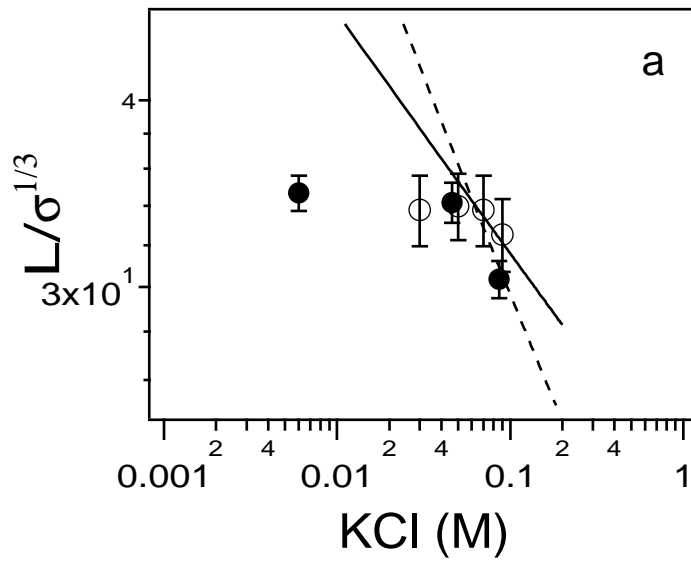


Figure 20.

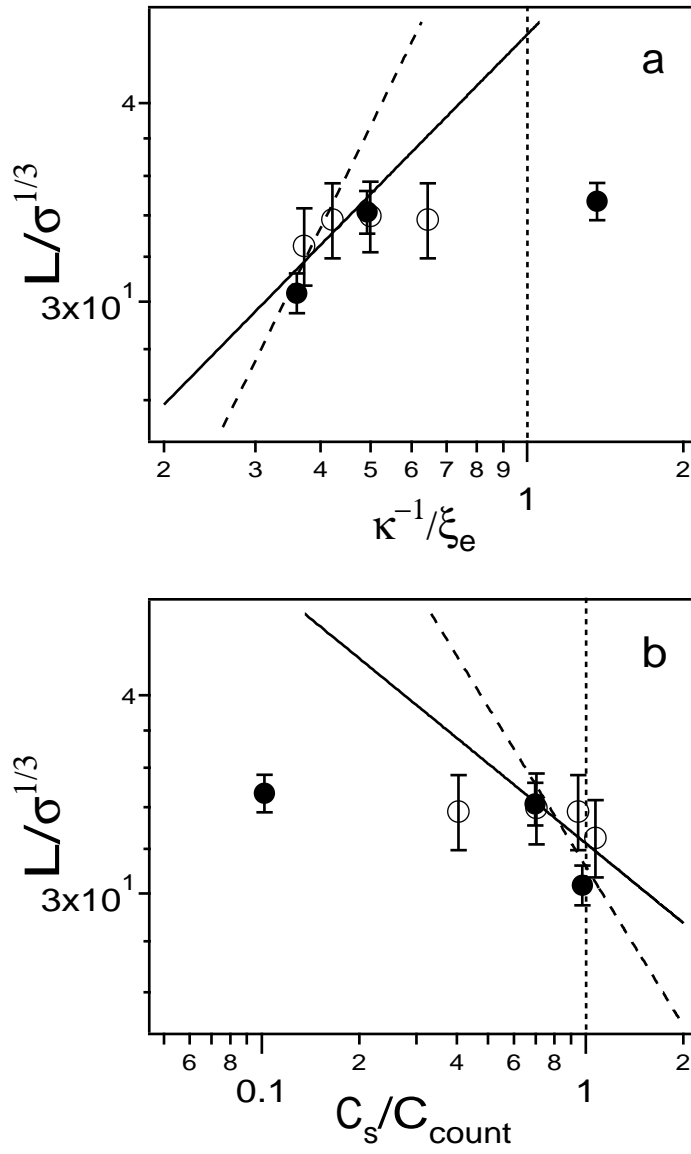


Figure 21.